Spring 2021

Enhanced Flow Boiling and Bubble Dynamics with HFE7100 & DI Water in Interconnected Microchannels

Jiaxuan Ma

ENHANCED FLOW BOILING AND BUBBLE DYNAMICS WITH HFE7100 & DI WATER IN INTERCONNECTED MICROCHANNELS

by

Jiaxuan Ma

Bachelor of Engineering
Dalian University of Technology, 2015

Submitted in Partial Fulfillment of the Requirements

For the Degree of Doctor of Philosophy in

Mechanical Engineering

College of Engineering and Computing

University of South Carolina

2021

Accepted by:

Chen Li, Major Professor

Jamil Khan, Committee Member

Yi Wang, Committee Member

Guoan Wang, Committee Member

Tracey L. Weldon, Interim Vice Provost and Dean of the Graduate School

DEDICATION

I would like to thank my family and friends, especially my parents, who support my study these years.

ACKNOWLEDGEMENTS

I want to thank the people involved in completing my project and, first foremost, express my deepest gratitude to my research supervisor Prof. Chen Li from the University of South Carolina. The guidance, attention to all the aspects of the work, and critique and assessment have led this research to its successful and fruitful results. I could not imagine any progress in the computation for design and optimization without your oversight. I would like to thank you for your inspiration to begin this research and the encouragement to carry on during the hard times. I am immensely grateful for the insights and knowledge Prof. Li shared on the subject matter. My praises and acknowledgment also give to Dr. Wenming Li and other lab mates from the Department of Mechanical Engineering of USC. Thank you all for the technical consultations and productive critics that led me to the completion of this project.

I would like to thank the fund supporting institute. The U.S. Department of Defense supported this work, Office of Naval Research under the Grants N000141210724 and N000141612307 (Program Officer Dr. Mark Spector). Devices were fabricated at the Institute of Electronics and Nanotechnology (IEN) in Georgia Tech, supported by the National Science Foundation under the Grant ECS-0335765. The author took the SEM images at USC Microscopy Center.

ABSTRACT

Flow boiling in microchannels using dielectric fluids is one of the most desirable cooling solutions for high power electronics. Primary two-flow patterns, including bubbly flow, slug flow, and annular flow, have been well established in microchannels. However, it is challenging to promote flow boiling performance, particularly critical heat flux (CHF), due to their unfavorable thermophysical properties. Considering these situations, flow boiling in parallel and isolated microchannels have been extensively studied.

In this dissertation, a novel concept that has five parallel microchannels (W=200 μm, H=250 μm, L=10 mm) are interconnected by micro-slots (20 μm wide and 250 μm deep) starting from the beginning section, and the middle section to the channel outlet have been proposed. The visualization study shows that these micro-slots designed as artificial nucleation sites can enable high-frequency nucleate boiling by drastically reducing the bubble waiting time and remaining the micro-slots entirely fully activated simultaneously. More importantly, such rapid switch on-off of uniquely coordinated nucleate boiling in the adjacent channels creates a highly desirable periodic rewetting mechanism to delay CHF conditions and enhance heat transfer rates substantially. Flow boiling in this innovative microchannel configuration has been systematically characterized with mass flux ranging from 462 $kg/m^2 \cdot s$ to 1617 $kg/m^2 \cdot s$. Compared to plain-wall microchannels with inlet restrictors (IRs), the flow boiling heat transfer coefficient (HTC) has a significant enhancement primarily owing to the enhanced latent heat transfer, including nucleate boiling and thin-film evaporation.

Moreover, CHF is substantially enhanced by ~76% at a mass flux of 1155 kg/m^{2}s owing to the rapid and periodic rewetting enabled by these micro-slots. Such drastic enhancements have been achieved without compromising the two-phase pressure drop. Based on the experimental studies of the novel design, a theoretical model and bubble dynamic studies are conducted to investigate the enhanced mechanism of flow boiling in the microchannel. The bubble dynamics have been systematically characterized in terms of bubble growth rates, bubble departure diameter, and bubble departure frequency, and thus nucleate boiling enhancement has been explained. The real time wall temperature for the present design fluctuates periodically and more stable compared to the chaotic fluctuation for the plain wall microchannel, which shows that micro slots can effectively manage the boiling instability. Furthermore, non-dimensional fitted correlations have been obtained to predict the bubble departure frequency and bubble departure diameter. The models and bubble dynamic studies provide insights into the enhanced HTC mechanism.

TABLE OF CONTENTS

LIST OF TABLES

LIST OF FIGURES

LIST OF SYMBOLS

A	Base area, m^2
A_c	Cross-section area, m^2
C_p	Heat capacity at constant pressure, J/kg·K
f	Frequency, Hz
G	Mass flux, $kg/m^2 \cdot s$
$\bar{h}$	Overall heat transfer coefficient, $W/m^2 \cdot K$
h_{fg}	Latent heat of vaporization, kJ/kg
H	Channel height, m
I	Electrical current, A
k	Thermal conductivity, W/m·K
L	Length, m
m	Parameter for fin efficiency
$\dot{m}$	Mass flow rate, kg/s
Na	Nucleation site density, $sites/cm^2$
Δp	Pressure drop, kPa
p	Pressure, kPa
P	Power, W
q''	Heat flux, W/cm^2
R	Electrical resistance, Ω

K	The slope of the linear function, Ω/K
δ	The thickness between heater and microchannel base, m
t	Time, s
T	Temperature, °C
$\overline{T}$	Overall temperature, °C
V	Electrical voltage, V
V	The volume of the bubble, m^3
W	Microchannel width, m
η	Efficiency
ρ	Density, kg/m^3
χ	Vapor quality

LIST OF ABBREVIATIONS

a	Ambient
b	Base
CHF	Critical heat flux
d	Departure
e	Exit
eff	Effective
Eva	Evaporation
f	Fin
g	Growing
HTC	Heat transfer coefficient
i	Inlet
nuc	Nucleate
s	Surface
sat	Saturated
sp	Single-phase
tp	Two-phase
v	Vapor
w	Waiting

CHAPTER 1 FLOW BOILING IN MICROCHANNELS

In two-phase flow cooling system, the heat generated in electronic devices (CPU, GPU, etc.) is dissipated by evaporation of a working fluid. This advanced thermal management solution can dissipate larger heat loads than the available traditional methods (liquid cooling or heat pipes) in a more efficient way. Two-phase flow boiling in microchannels is one of the most promising cooling techniques for microelectronics.

Moreover, in two-phase flow, the total pressure drop includes acceleration pressure drop and friction pressure drop was significantly increased, due to the existence of acceleration pressure drop. In addition, bubble dynamics plays an essential role in the cooling application of two-phase flow boiling. It can significantly be influenced by bubble shape and channel size [1]. In this proposal, the literature review focuses on the following aspects, including the two-phase flow boiling in microchannels and the bubble dynamics.

1.1 Flow Patterns in Microchannels

Two-phase microchannel heat sinks are among the strongest candidates for heat removal devices in high heat flux environments by their large surface area to volume ratio, compact dimensions, and low flow rate requirements [2]. The accurate prediction heat transfer coefficient of flow boiling in a microchannel has recently served as essential design guidance for various cutting-edge technologies [3]. Due to the intense heat removal from tiny areas [4-8], the volume available for packaging cooling hardware has averted stringent limits. However, the heat transfer correlations design commonly used by engineers for the

thermal design was established over the past decades for the conventional nuclear power generation and petroleum industries.

Compared with pool boiling phenomena, flow boiling has the liquid flow on the micro level. Flow boiling can be triggered by liquid density difference leading to the natural circulation of fluid or external force, result in forced movement. The types of two-phase fluid flow during the flow boiling are more complicated than the pool boiling. The simplest and most common way of dealing with flow boiling heat transfer is using single-phase and pooling boiling of superposition [9, 10].

Two-phase liquid flowing in a tube expresses various flow structures depending on different phase interfaces [11, 12]. While the liquid is heated and evaporated, the liquid and vapor also have other flow structures. The main characteristic of two-phase flow is an existing interface between the two-phase fluids, especially in the liquid-gas two-phase flow. In general, surface tension significantly helps develop the bending interface to form a sphere, such as bubbles or droplets. The sphere structure maybe transforms due to the discontinuous variation interface in a continuous phase, which could lead to even more significant change of a sphere structure. Therefore, small bubbles could shape well into the globe. However, it should be noted that large bubbles could transform quickly.

In order to better understand the flow characteristics and flow boiling mechanisms, two-phase flow patterns have been observed visually. The primary two-phase flow patterns, including bubbly flow, slug flow, and annular flow, have been well established in microchannels [12, 13]. As shown in Figure 1.1, at the initial stage (single-phase), the subcooled working liquid enters from the inlet. As the fluid heated up, the wall temperature approached saturation temperature. Meanwhile, subcooled boiling began. At this stage,

individual bubbles start to form at bubbly flow with smaller bubble diameters than hydraulics diameter. The convective boiling process passes through bubbly, plug regimes. The increase of heating power induced the annular flow, moreover, the rapid vigorous generation of vapor, leading to the elongated bubbles formed, the local dryout of the microchannel occurs at the top of the channel, where the liquid film would become thinner on account of gravitational force, and the dryout then progresses around the perimeter from top to bottom along the channel.

In addition, Figure 1.1 indicates schematically the sequence of regimes associated with subcooled boiling. In the fully developed nucleate boiling regime, the nucleate boiling mechanism generally is so robust that it completely dominates the heat transfer process. At higher flow velocities and subcooling levels, convective effects could be significant well beyond the point where the nucleation site density has attained a level equal to that for pool boiling at the same superheat.

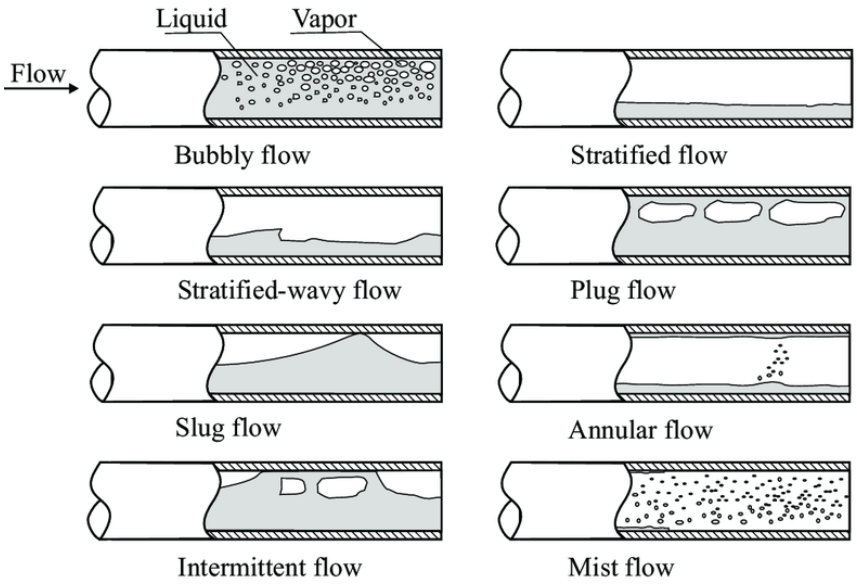

Figure 1.1 Two-phase flow patterns for flow boiling [13].

1.2 Instabilities of Two-Phase Flow Boiling in Microchannels

Generally, the two-phase flow instabilities for boiling in microchannel demonstrate an essential subject in the last thirty years. There are still practical problems with heat exchange equipment, such as the evaporator, nucleate reactor, cryogenic equipment, and chemical equipment. The negative consequences of two-phase flow instabilities are mechanical vibration, which will lead to fatigue damage for the device, control system interference, periodical change of the local thermal stress that causes heat transfer deterioration. Therefore, the investigation of two-phase flow instabilities is the principal occurrence factor of understating the result in the unsteady flow. It is challenging to prevent the two-phase flow instabilities and determine the critical value for which flow instabilities occur.

Ledinegg [14] first investigated the two-phase flow instabilities experimentally the method, and the results indicated that the flow and pressure difference were not following monotropic function. In 1983s, Wissler [15] studied the instabilities under the natural circulation boiler, using the homogenous flow model. Wallis and Heasley [16] established a solution to integrate the continuity equation and the energy equation. Quandt [17] presented the experimental data for the parallel channel stability (up to 110 bar). The study indicated that the flow pulse occurred in the subcooled area at a particular heat load and heat flux. In the meantime, due to the simplifying assumptions, deep understandings are still needed to narrow the gap between analysis results and experimental data.

Nevertheless, the studies have common agreements over the causes of two-phase flow instabilities and the consequences, including temperature fluctuations, pressure difference, backflow, local dryout and CHF. Researches identified that flow instabilities could be triggered by mass flow rate, flow regimes, bubble dynamics, subcooling liquid

and coolant properties. In recent years, many efforts have been taken in order to overcome the flow instability issues. Table 1.1 listed various of researches that focused on two-phase flow boiling instabilities in microchannels in recent years.

Table 1.1 Two-phase flow boiling instabilities in microchannels

Author	**Key Parameters**	**Major Results**
Kuang, *et al.* [18]	Pressure drop System pressure Wall temperature	The unstable oscillation occurred due to the pressure drop will decays as the wall temperature of the evaporator gets close to the liquid temperature.
Alugoju, *et al.*[19]	Divergence angle Width ratio (outlet to inlet)	Diverging microchannels have a better performance to control flow instability compared with straight channels.
Xu, *et al.* [20]	Temperature oscillations Pressure oscillations	Two-phase flow instability modes have been identified with long/short-period and large/small-amplitude.
Ozdemir, *et al.* [21]	Inlet/outlet temperature Pressure fluctuations Wall temperature	Upstream compressibility can take account of flow reversal in microchannels.
Huang, *et al.* [22]	Pressure drop Boiling number	The oscillation period of flow instability has a strong bearing on the boiling number.
Chen, *et al.* [23]	Wall temperature Flow rate Compressible volume	The reverse flow was observed at low pressure circulation, long two-phase region and upstream compressible volume.
Chen, *et al.* [24]	Ledinegg instability Density wave Pressure drop	The characteristics of three types of the instability of liquid nitrogen have been numerically studied and compared with those of water/refrigerant fluids.

Cui, *et al.* [25]	Pressure oscillations Heat transfer coefficient Flow rate Jet-to-target distance	The characteristics of two-phase flow instability in distributed jet array impingement boiling of HFE-7000 on pin-fin surface and its affecting factors have been investigated experimentally.

1.3 Flow Boiling in Microchannel with Deionized Water

Phase change heat transfer, primarily flow boiling in microchannels, is among the most promising cooling solutions of high-power electronics [26, 27]. Owing to the potentially high heat transfer rate for flow boiling in horizontal microchannels, several experimental investigations of flow boiling in microchannels have been conducted over the last decades. Many researchers have found that flow through the channel during flow boiling in microchannels was conventional or oscillations [28]. However, it is challenging to enhance flow boiling in an isolated parallel microchannel due to the unstable non-uniform distributions or maldistribution of two-phase flow, resulting in the dryout, which could lead to the possible device failure [29]. In parallel channels, the unbalanced two-phase flow distribution can result in degradation of boiling performance and a sharp increase in surface temperatures [30]. It is incredibly challenging to forbid local dryout near the outlet section of horizontal microchannels because of the limit for liquid supply improvement.

The results of recent studies suggest that the severe flow instabilities indicated by large amplitude wall temperature and pressure oscillations can deteriorate heat transfer coefficient (HTC) and critical heat flux (CHF) as well [31]. In general, the main efficient heat transfer modes including nucleate boiling, convection, and evaporation have been impeded due to the lack of liquid supply. As mentioned above, some earlier studies have

concluded that the enhancement of nucleation boiling and thin-film evaporation is cracid [32-34]. In the last decades, numerous techniques have been explored to improve the heat transfer performance of flow boiling in microchannels. Many designs [35-37] are widely used to promote the flow boiling performance, such as inlet restrictors (IRs) [38]. The primary mechanism is to use this configuration to suppress liquid backflow to enhance the flow instabilities. The reentrant cavities [39] are designed as nucleation sites to improve active nucleation site density in enhancing the nucleation boiling, the impingent jet [40]. The mechanism is jetting the fluid onto a hot surface to cool the surface. In addition, the micro pin fin [41] array at the bottom and the nanowires [26] in the microchannel are designed to improve nucleation boiling. Table 1.2 has shown the studies of traditional techniques in flow boiling.

Moreover, flow boiling can significantly improve the heat transfer efficiency, enhanced nucleation boiling, and decrease the coolant needed [28]. For example, multiple jets with reentry cavities take advantage of the utility of high latent heat of vaporization associated with typical liquid-vapor phase change phenomena, allowing significant heat transfer with little temperature rise. Kosar and Kuo found inlet orifices placed inside parallel microchannels could suppress the boiling flow instabilities [42]. HTC and CHF were successfully enhanced by regulating bubble slugs. However, the increased pressure drop may cause higher power and required a high flow rate. Kuo and Peles [43] presented a new microchannel with reentrant cavities to promote the generation of bubble nucleation and uniformity. A vast bubbly region at high mass velocity was observed and significantly reduced. Wang and Zhang [44] employed the impingement jets to reduce wall superheat and achieve higher heat removal rates, although this technology required additional pump

power. Stroock and Dertinger [45] indicated that chaotic mixer in microchannels with DI water is a passive method for mixing steady pressure-driven flow streams in microchannels at low Reynolds number. But it hadn't been studied to enhanced two-phase transport in the silicon area. However, the enhancement can only be triggered at a low heat flux. As long as the heat flux increasing, the proportional energy of nucleation boiling decreased due to the lack of liquid rewetting and resulting in local dryout at the outlet section of microchannels. Sustained nucleate boiling can promote heat transfer rate and maintain the wall temperature at a safe level [29].

Another crucial aspect of flow boiling is the critical heat flux (CHF), showing the safe operation margin of high power density electronics [46]. The crisis reason for boiling, which results in electronic devices failure, is overheating—the liquid rewetting ability, incredibly close to the outlet section of microchannels, thoroughly determined the CHF. Many microchannel configurations have been developed to enhance CHF using DI water as working fluid significantly. These include controlling reversal vapor flows by inlet restrictors (IRs) [47], recovering pressure by tapered channels [48], improve surface wettability by decorating micro/nanostructure [26, 27, 49-51], and promoting liquid rewetting by capillary micro/nanostructures [52-55]. Wang *et al*. [56] reported an ultrahigh CHF over 1.2 kW/cm^2 has been achieved by improving the thin film evaporation boiling with nanoporous membranes. In this study, the thickness of the liquid film gradually reduced along with the heat flux increased. However, about 1.8atms were applied to serve as the driving force to pump working fluid through the membranes. As aforementioned in the previous study [57], a maximum of 1015W/cm^2 has been achieved via enhancing liquid supply to delay local dryout at outlet section of microchannel at a mass flux of 680 kg/m^2

without raised two-phase pressure drop significantly. A high CHF of 830 W/cm^2 is recently revealed at a low mass flux of 396 kg/m^2 in microchannels with capillary micro-pinfin fences.

Table 1.2 Studies of traditional techniques in flow boiling

Author	**Methods**	**Pros**	**Cons**
Kosar and Kuo (2006) [58]	Inlet restriction	Enhanced HTC and CHF Regulating bubble slugs Suppress flow oscillations	Increased pressure drop Required higher flow rate
Kandlikar, *et al*. (2005) [59]	Inlet restriction	Reduced the instabilities	Increased pressure drop
Wang, *et al*. (2008) [47]	Inlet restriction	Reduced amplitudes of temperature and pressure oscillations	Higher pressure drop and lower HTC at high vapor quality.
Kosar and Kuo (2005) [60]	Reentrant cavities	Enhanced capillary flow Enhanced HTC	CHF enhancement are insignificant
Kuo and Peles (2008) [39]	Reentrant cavities	Enhanced nucleation site distribution An extended bubbly region was observed in high mass velocity. Significant reductions in the wall superheat.	Effected the CHF enhancement.
Xia, *et al*. (2010) [61]	Reentrant cavities	Reduced the friction factor	Augment pressure drop
Morsged, *et al*. (2012) [26]	Nanowires	Reduced surface superheat for ONB Enhanced heat transfer rate in single-phase	Pressure fluctuation increased

Krishnamurthy and Peles, (2008) [62]	Micro pin fins	Enhanced CHF & HTC Promote capillary flow Observed flow patterns	Additional pressure drop
Stroock and Dertinger, (2002) [63]	Micro mixer	Mixing steams at low Re	It hasn't been studied for enhanced two-phase transport in silicon.
Wang and Zhang, (2004) [44]	Impingement jets	Reduce wall superheat Achieve higher heat removal rates	Required additional pump power

1.4 Flow Boiling in Microchannel with Dielectric Fluids

Compared to deionized (DI) water, properties of dielectric fluids are more stable and reliable for applications of electronics cooling [64-66], which make dielectric fluid flow boiling in microchannels a more favorable cooling solution for high power electronics. However, considering their unfavorable thermophysical properties, enhancing flow boiling heat transfer coefficient (HTC) and critical heat flux (CHF) in microchannels is a challenging task. For instance, the thermal conductivity of HFE-7100 is 0.069 W/m·K, approximately ~10 times lower than that of water (~0.6 W/m·K). Besides, the latent heat of vaporization of HFE-7100 is 111.6 kJ/kg, nearly 20 times smaller than that of water. In addition, the surface tension is 13.6 mN/m, five times lower than that of water, making it difficult to form and sustain long thin liquid films on heated surfaces. On a highly wetting fluid, it is challenging to promote efficient thin film evaporation and nucleate boiling. Table 1.3 shows the more details about major thermo-physical properties of HFE-7100.

Many efforts have been taken to enhance flow boiling HTC on dielectric fluids. For example, nanowires [65], reentrant cavities [66, 67], porous graphite [36, 68] and other

porous surfaces [69] can effectively enhance nucleate boiling by increasing nucleation site density. In addition, sustaining thin film through enhanced capillary flows induced by micro/nano-structures can result in highly efficient thin film evaporation [67]. Other methods including diverging microchannels [37], inclining microchannels [70], and mixing generation [67] have been developed to significantly promote HTC of HFE-7100 flow boiling.

Table 1.3 Major thermo-physical properties of HFE-7100

Name	**HFE-7100**
Latent Heat of Vaporization (kJ/kg)	111.6
Specific Heat, 25 °C, 1 ATM (J/kg·K)	1183
Liquid Thermal Conductivity (W/m·K)	0.069
Boiling Point, 1ATM (°C)	61
Liquid Density, 25 °C (kg/m3)	1520
Kinematic Viscosity (cSt)	0.37
Surface Tension, 25 °C (mN/m)	13.6
Vapor Pressure, 25 °C (kPa)	26.9

However, it is more challenging to enhance CHF of dielectric fluid flow boiling in microchannels. CHF crisis in a closed microchannel system can be triggered by three main factors, such as explosive boiling, two-phase flow instabilities, and local dryout. Low thermal conductivity of dielectric fluids is more likely to trigger explosive boiling and result in premature CHF conditions. Local dryout in the form of a stable vapor film on heating surfaces is highly likely to occur at low surface tension dielectric fluids due to its weak capillarity. Moreover, severe two-phase flow instabilities [71, 72] can also lead to

local dryout, especially pounced near the outlet section. Enhancing CHF on DI-water with numerous technologies, such as regulating bubble slugs [73], suppressing flow instability [74], modifying surface properties [27, 49, 50], and promoting liquid rewetting [52-55] have been studied for decades. Noting that research to enhance CHF on dielectric fluid at room temperature is few. For instance, the enhancement of HTC in microchannels with nanowires [65], reentrant cavities [66] has been achieved, but not on CHF. One of the main reasons for the limited enhancement of CHF is the lack of liquid supply, despite that capillary flow is promoted by integrating reentrant cavities [66] and nanowires [65]. As aforementioned, Lee *et al*. have reported a high CHF of ~700 W/cm^2 at a high mass flux of 5550 kg/m^2 s on pre-cooled HFE-7100 in microchannels with the inlet temperature of -30^oC [75]. In general, it is extremely challenging to enhance CHF in dielectric fluid flow boiling with inlet temperature at room temperature.

1.5 Bubble Dynamics in Microchannels

The enhancement mechanism to enhance nucleation boiling is equally vital in flow boiling heat transfer study in microchannels. The bubble dynamic study is one of the most critical issues. In the last decades, the bubble dynamics study has emerged as a boiling heat transfer subdiscipline. The primary research usually forced on the growth and motion pattern of vapor bubbles. Moreover, bubble growth and departure from a heating surface have magnificent implications for the heat transfer mechanism of nucleate boiling.

Since the 1950s, single bubble dynamics has already made significant progress, and various theoretical models have been gradually developed. Many experimental data have been accumulated. It promoted the development of nucleate boiling heat transfer mechanism. However, especially on bubble-bubble interaction, there is not a satisfactory conclusion when considering multiple bubble system.

As a previous analysis [76], the nucleate bubble forming on an active cavity continues to grow under various forces. At the initial stage, the vapor pressure inside the bubble is satisfied $p_v > p_l + \frac{2\sigma}{r}$. Vapor bubbles begin to grow up because of the unbalance between the surface tension and the difference of pressure inside and outside the vapor bubble. During this period, the temperature inside the vapor bubble is equal to the surrounding liquid, bubble growth is subject to surface tension force and inertia force, and the growth rate is very high.

With the volume of vapor bubble increased, the effect of surface tension decreases. The pressure inside the vapor bubble is close to the outside, and the vapor bubble grows under the isobaric condition. The bubble temperature is equal to the saturated temperature under the system pressure. At this stage, the heat transfer process from superheated liquid to the vapor bubble dominates the bubble growth, growth rate reduced, and bubble duration has enhanced.

To better understand the pattern of bubble growth and motion [77-79], two different situations need to be concerned, bubble growth under superheated liquid with uniform temperature and bubble growth with the non-uniform temperature of different boundary conditions. The violent oscillation of the bubble formed from flow boing heat transfer has been investigated analytically and numerically. Meanwhile, only a limited number of papers try to examine the combined work of bubble dynamics and microchannels.

This study has formulated a general bubble dynamics model, especially in bubble departure diameter, bubble departure frequency, and bubble growth diameter, suitable for the oscillating bubble formed in microchannels for high heat flux heating and rapid and high-frequency alternating nucleation boiling circumstances. A nondimensional

correlation is established for different working fluids, and mass flux is using experimental data.

With uniform density and temperature distribution approximation, the estimated values of the far-field pressure signal from the evolving bubble formed from the fully evaporated droplet are in good agreement with experimental results. In this dissertation, a semi-theoretical model has been developed to analyze the bubble departure diameter, bubble growth diameter, and bubble departure frequency. Multiple bubbles are considered for flowing boiling at low heat flux conditions. A comparison of bubble departure diameter, bubble growth rate, and frequency with various working conditions are made with well-controlled experiments.

1.6 Bubble Dynamics Models

Flow boiling in a microchannel is characterized by nucleation rate and dynamic behavior of vapor bubbles in the channel [7, 80, 81]. Many researchers have identified the bubble dynamics play an essential role in flow boiling heat transfer [82-84]. In the last decades, the dynamics of vapor bubbles formed on a heated surface subjected to forced flow have been studied [85]. Flow boiling in microchannel involves many complex phenomena such as bubble nucleation, growth, departure, and coalescence. Bubble dynamics are fundamental to the understanding of boiling heat transfer mechanism and prediction of heat transfer. It concerns bubble generation, bubble growth, bubble collapse, a departure from nucleation sites, bubble motion through fluid, forces acting on the fluid, and heat transfer performance.

Moreover, nucleation site density depends on the surface physical properties, surface finish, liquid physical properties, heat flux, and the wall superheat [86]. Vapor bubble growth is determined by the surface tension, liquid inertia, and difference between

the pressure within the bubble and external pressure. Bubble departure is related to the surface tension and liquid resistance on the bubble due to asymmetrical bubble growth, acting opposite to the fluid motion [28]. Several studies have been developed to predict the bubble growth rate, bubble departure frequency, and bubble departure diameter by calculating various forces that act on the growth bubble from a heated surface. However, there are a few correlations or models that could be widely applied to two-phase flow boiling in microchannels with HFE-7100. These limitations indicate a challenging task to develop a numerical technique for two-phase flow with the various interface. The shape and movement of the interface and each geometric configuration of phase need to be computed as part of the solution. The large property jumps associated with phase change also increase the complexity of the solution method. Therefore, future work is still needed to investigate a more reliable model to predict bubble dynamics.

Table 1.4 listed correlations for the departure diameter of bubbles during nucleate boiling over the past seventy years. In many experimental studies, the departure diameter was generally determined from the movies captured by high-speed camera. Based on data obtained in this manner, several correlation equations have been proposed.

The correlations are written in terms of the departure Bond number Bo_d defined as

$$Bo_d = \frac{g(\rho_l - \rho_v)d_d^{\,2}}{\sigma} \tag{1}$$

Gunther [87] was one of the earliest authors to study nucleate boiling under forced convection conditions. The research with high speed and resolution photographic method has been developed for the forced convection boiling of heat transfer. It shows that the bubble size and bubble lifetime reduced as the bulk fluid velocity increased. Fritz [88] found that the bubble departure diameter is related to surface tension and buoyancy force.

Klausner *et al.* [89] proposed a prediction model for bubble departure diameter with various forces acting on the growing bubble. Core and Rohsenow [90] analyzed the correlation of bubble departure diameter. However, it only meets the cases for low pressure.

Moreover, Zeng *et al.* [91] developed an improved model that the growth force is dominant compared to the surface tension force near the departure point. Thorncroft and Mei [92] correlated the data for bubble departure diameter by founding the bubble growth increases with Jacob number (growing ΔT_{sat}) under otherwise identical conditions in up-flow or downflow. J.F. Klausner [89] have proved the surface tension alone cannot prevent the vapor bubble from departing. Situ *et al.* [93] focused on bubble lift-off size in subcooled flow boiling, taking into account the force balance analysis, which showed that the bubble is governed by growth force and shear lift force at the instant of the lift-off.

Table 1.4 Departure diameter correlations [28]

Equations	**Authors**
$Bo_d^{1/2} = 0.0208\theta$	Fritz (1935) [94]
$Bo_d^{1/2} = \left[\frac{\sigma}{g(\rho_l - \rho_v)}\right]^{-1/6} \left[\frac{6k_l(T_w - T_{sat})}{q''}\right]^{1/3}$	Zuber (1965) [95]
$Bo_d^{1/2} = \left[\frac{3\pi^2 \rho_l \alpha_{T1}^2 g^{1/2}(\rho_l - \rho_v)^{1/2}}{\sigma^{3/2}}\right]^{1/3} Ja^{4/3}$ $Ja = \frac{\rho_l C_{pl}\left[T_w - T_{sat}(P_\infty)\right]}{\rho_v h_{lv}}$	Ruckenstein (1964) [96]
$Bo_d^{1/2} = 0.04Ja$	Core (1969) [90]
$Bo_d^{1/2} = C(Ja^*)^{5/4}$ $Ja^* = \frac{T_c C_{pl}\rho_l}{\rho_v h_{lv}}$	Rohsenow (1969) [97]

$C = 1.5\times10^{-4}$ for water $C = 4.65\times10^{-4}$ for fluids other than water $Bo_d^{1/2} = 0.25(1+10^5 K_1)^{1/2}$ for $K<0.06$	
$K_1 = (\frac{Ja}{\mathrm{Pr}_l})^2\{[\frac{g\rho_l(\rho_l-\rho_v)}{\mu_l^2}][\frac{\sigma}{g(\rho_l-\rho_v)}]^{3/2}\}^{-1}$	Kutateladze and Gogonin (1979) [98]
$d_d = 0.25\sqrt{\frac{\sigma}{g(\rho_l-\rho_v)}}[1+(\frac{Ja}{\mathrm{Pr}_l})^2\frac{1}{Ar}]^{1/2}$ $5\times10^{-7} \le (\frac{Ja}{\mathrm{Pr}_l})^2\frac{1}{Ar} \le 0.1$ $Ar = \frac{g\rho_l^2}{\mu_l^2}(\frac{\sigma}{g\rho_l})^{3/2}$ is the Archimedes number	Stephan and Abdelsalam (1980) [99]
$d_d(\frac{P_c M}{K_B T_c})^{1/3} = 5.0\times10^5(\frac{P}{P_c})^{-0.46}$ $Bo_d^{1/2} = 0.19(1.8+10^5 K_1)^{2/3}$	Jensen and Memmel (1986) [100]

In addition, in order to introduce more recent results on bubble departure diameter, Chen and Groll [101] developed a novel method to simulate existing bubble shapes by solving the Yong-Laplace equation. Besides, Helden et al. [102] performed the bubble departure diameter variation and depicted that the bubble departure diameter decreased as the liquid velocity increased. Chen and Ren [103] proposed a prediction model for the bubble departure diameter based on force analysis and found that the contact circle diameter of vapor bubble is more extensive for a bubble with a bigger departure diameter. Phan [104] considered a model considering the effect of contact angle on bubble departure diameter during heterogeneous boiling. Koncar *et al.* [105] concluded the variation of

bubble diameter according to local flow conditions at low pressure in upward subcooled flow. Mazzocco *et al.* [106] was modeling the relative velocity of the bubble to improve the lift-off diameter predictions.

To predict the bubble departure frequency, Cole [107] indicates that buoyancy force and drag forces could dominate in the hydrodynamic region if the bubble departure diameter and bubble frequency are equal to the bubble rise velocity. Hatton and Hall [108] proposed the correlation of bubble departure frequency and bubble departure diameter. Ivey [109] suggested the relationships between bubble frequency, bubble departure diameter, and rise velocity in nucleate boiling. Tu and Yeoh [110] determined the relationship between bubble departure diameter and bubble frequency at low-pressure subcooled boiling flows. Lee *et al.* [111] briefly introduced the bubble frequency is correlated with bubble departure diameter with a form of $f \cdot D^n = const$. Zuber *et al.* [112] proposed a relationship between the product of bubble frequency and diameter in terms of fluid properties, the bubble rise velocity is

$$\mathrm{D}_d / t_G \tag{2}$$

Where,

$$t_G = t_W \tag{3}$$

Figure 1.2 shows the model validation with other correlations, and it is observed that the model predictions do not agree well with the present experimental data. In this study, the comparison of experimental data with different models predicted of bubble departure frequency and bubble departure diameter in the last decade is plotted in Figure 1.2. As shown in Figure 1.2 (a), the present study of experimental data has the better performance of departure frequency, and the maximum frequency has achieved a value of

~7700 kHz at a heat flux of 33 W/cm^2. Figure 1.2 (b) shows that the experimental data of bubble departure diameter is much higher than the developed prediction models. However, it is still hard to illustrate a clear trend due to the significant variations in the experimental conditions and the microchannel dimensions. Therefore, the non-dimensional analysis is used for establishing a prediction model in this dissertation proposal.

Table 1.5 Present bubble dynamic models and existing models/correlations [113]

Flow conditions	**Parameters**	**Author**	**Major assumptions**
Pool boiling	Bubble departure frequency	Cole (1967) [107]	The hydrodynamic region where buoyancy and drag force dominates.
Pool boiling	Bubble departure frequency	Ishii and Zuber (1979) [114]	D_d/t_G= bubble rise velocity; $t_G=t_W$
Pool boiling	Bubble departure frequency	Ivey (1967) [109]	Buoyancy and drag forces dominate
Forced convective boiling	Bubble waiting time	Basu *et al.*(2005) [115]	Correlated with wall superheat.
Forced convective boiling	Bubble growing time	Basu *et al.* (2005) [115]	Correlation with departure diameter, wall superheat and bulk subcooling.

Many new concepts are demonstrated to enhance critical heat flux and heat transfer coefficient, suppress flow instabilities and improve nucleation boiling. Although the early results have shown the enhancement of flow boiling heat transfer in micro-slots

microchannels by enhancing nucleation sites to enhance and sustain nucleation boiling and eventually improving HTC and CHF, the enhanced mechanisms of heat and mass transfer leading to high HTC and CHF are not well understood yet. Therefore, theoretical models of bubble dynamics are essential to deepening understanding. For theoretical bubble dynamic models based on the observed new phenomenon, more data should be collected to compare with differently structured microchannels with different working fluids to get more accurate and reliable results. Table 1.5 shows the present bubble dynamic models and existing models/correlations. More visualization study is needed to get accurate trends for bubble growth, departure diameter, departure frequency, and switch frequency for the interconnected microchannels configuration in this dissertation compared with the aforementioned various bubble dynamic models.

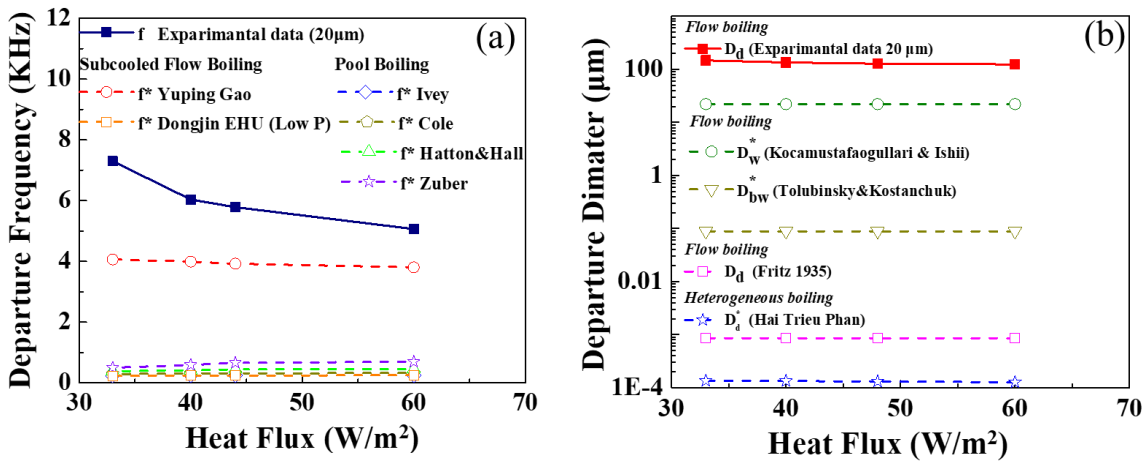

Figure 1.2 (a) Data comparison of bubble departure frequency as a function of heat flux. (b) Data comparison of bubble departure diameter as a function of heat flux.

To summarize existing works in two-phase flow boiling in microchannels, improvements on HTC and CHF are achieved by improving nucleate boiling, thin-film evaporation, flow mixing, flow stabilities delay the surface dryout. However, backflow and instability occur during flow boiling in microchannels resulting in non-uniform flow and

low heat transfer, such as additional pressure drop, complex system, low energy efficiency, and explosive boiling.

This dissertation includes three parts to understand and model the two-phase flow boiling heat transfer in the novel designed interconnected microchannels. Part I of this dissertation discussed the experimental methods used and key trends of heat transfer coefficient with different mass velocity and working fluids with innovative microchannels configurations. Part I also included the bubble dynamics study and proportional energy study to investigate the mechanism of enhancing heat transfer performance. Part II focuses on the effect of different sizes of micro-slots to improve the design as mentioned above and enhanced CHF and HTC. The unique features of micro-channel flow boiling are discussed in Part I and II, and Part II is carefully identified and incorporated into the model of Part III. Three empirical correlations have been proposed using the experimental results from Part I and II.

CHAPTER 2 HIGHLY COORDINATED, RAPID AND SUSTAINABLE NUCLEATE BOILING IN MICROCHANNELS ON HFE-7100

This study presents an innovative microchannel configuration with 28 micro-slots interconnected on each parallel channel to enhance nucleate boiling and CHF. Micro-slots served as active nucleate sites that aim to improved nucleation boiling of heat transfer. Moreover, significant progress has been made in the two-phase flow boiling of microchannels, several new phenomena such as bubble switch in microchannels, thin liquid film inhales in micro-slots, and high-frequency rewetting with micro slots have been observed by visualization study with a high-speed camera, which results in the nucleate boiling improvement.

With the enhancement of the liquid supply at microchannels, a significant delay of CHF crises can be generated in the present configuration of interconnected microchannels with a slightly reduced two-phase pressure drop. HTC can be magnificently enhanced due to the thin film evaporation and nucleate boiling enhancement by micro-slots. In additional, bubble dynamics study and proportional energy study will be adopted to study the enhanced mechanism of the present design interconnected microchannels compared to the plain wall microchannel configuration with inlet restrictors. Moreover, the dominant energy of heat flux will be explored in this study.

2.1 Design and Microfabrication of Interconnected Microchannels

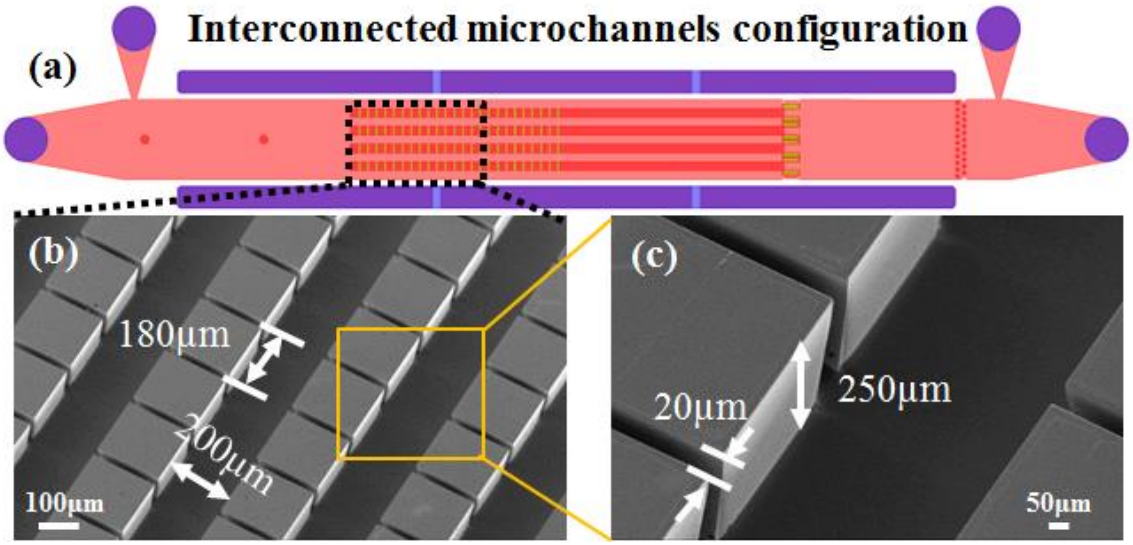

Figure 2.1 (a) Configuration of the interconnected microchannels. (b, c) Scanning electron microscopy (SEM) images of interconnected microchannels and dimensions.

An innovative microchannel configuration has been developed to enhance flow boiling in terms of HTC and CHF on HFE-7100, as shown in Figure 2.1. In this design, five parallel microchannels are interconnected by 28 micro-slots on each intermediate wall. These micro-slots were designed as nucleation sites to enhance and sustain nucleate boiling. More details about the dimensions of microdevice have been discussed in our previous study [116]. More importantly, nucleate boiling in neighboring microchannels can be harmonically coordinated for the first time, leading to significantly higher bubble growth rates and rewetting frequency and, eventually, greatly enhanced HTC and CHF.

In plain wall microchannels, it is challenging to enhance heat transfer performances of flow boiling due to a long waiting time for bubble nucleation and bubble departure time. Figure 2.2 shows the experimental setup and the test package module. The test setup consists of an optical imaging system, a data acquisition unit, and an open coolant loop. HFE-7100 is pumped by pressurized nitrogen (N_2). All test processes are executed at room

temperature ~ 19 ºC and 1 atm. Details of the experimental setup were reported in our previous studies [67].

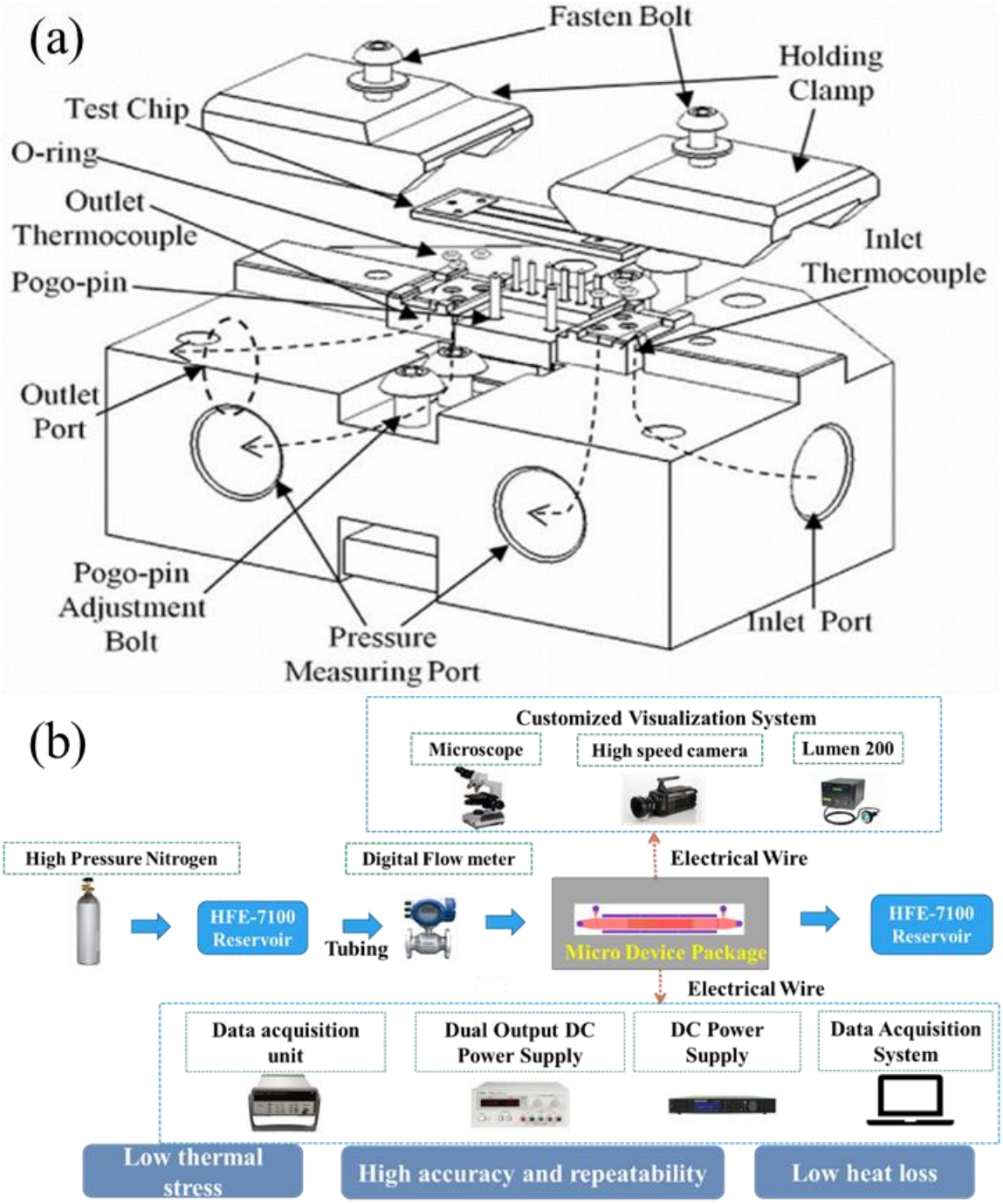

Figure 2.2 (a) An exploded 3D model of the test package module [117] and (b) experimental setup.

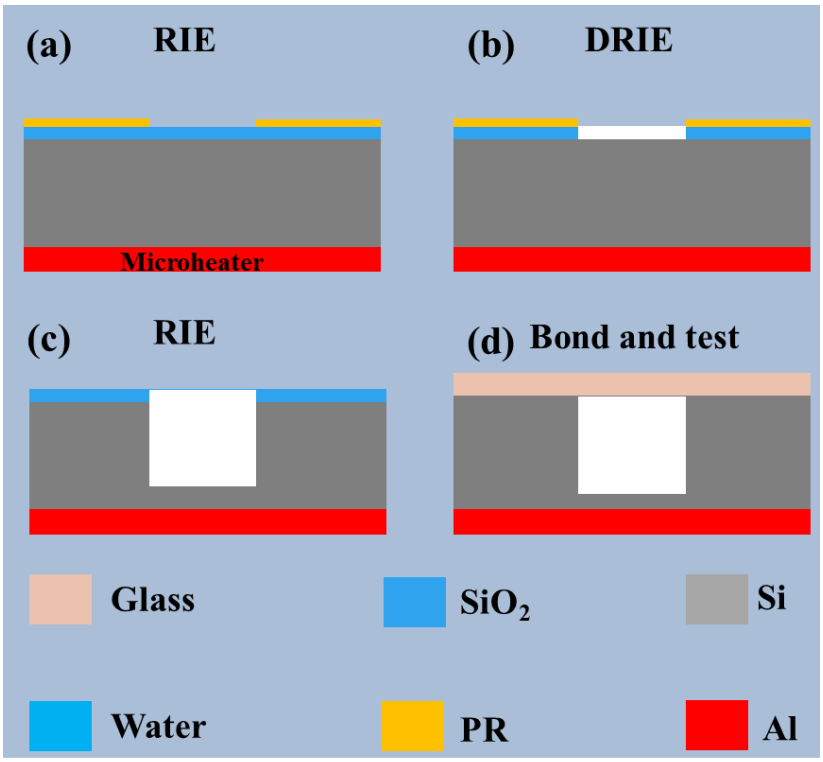

Figure 2.3 Microfabrication process of the tested microdevice.

Figure 2.3 shows the detailed flow chart to fabricate the microfluidic device. First, 1 ± 0.01μm thick thermal oxide layer was grown on both sides of n-type <100> silicon wafer to provide electrical insulation for the micro heaters and serve as a hard mask for deep reactive ion etching (DRIE). A 1 ± 0.05μm thick, thin-film micro-heater was fabricated through a lift-off process on the backside of the wafer. Silicon oxide serving as an etching mask was etched off using reactive ion etching (RIE). Then five parallel micro-channels were etched by DRIE. The depth of the channel is 250 ± 3μm. The DRIE process also creates deep vertical sidewalls with a root mean square (RMS) roughness of ~300 nm. A Pyrex glass wafer was anodically bonded to the silicon substrate to seal the microfluidic device. The individual microchannel test chips (length 30 ± 0.005 mm; width 10 ± 0.005 mm; thickness 1 ± 0.005 mm) were cut from the wafer by a dice saw. More detailed microfabrication was elucidated in our previous study [116].

2.2 Data Reduction

In experiments, the input power was calculated by multiplying the DC voltage (V) with current (I). Then the effective heat flux was calculated after subtracting the heat loss, Q_{loss}, (pre-calibrated between the ambient environment and the test device) from the total input power, P, as follow,

$$q''_{eff} = \frac{P - Q_{loss}}{A} \tag{4}$$

where A is the base heating area. Based on the pre-calibrated linear relationship between temperature and electrical resistance, the average temperature of the microheater (on the backside of the device) was calculated as,

$$\bar{T}_{heater} = K\left(R - R_a\right) + T_a \tag{5}$$

R_a is the resistance of microheater at ambient temperature T_a and K is the slope of pre-calibration. The average temperature at the bottom wall of microchannels was then derived as,

$$\bar{T}_{wall} = \bar{T}_{heater} - \frac{q''_{eff}\delta}{k_s} \tag{6}$$

Where δ and k_s are the substrate thickness, the thermal conductivity of silicon, respectively.

The fin efficiency, η_f, of a finite fin was estimated from

$$\eta_f = \frac{\tanh(mH)}{mH} \tag{7}$$

The equation of η_f is used to characterize fin performance and to calculate the average effective HTC, where the parameter m was calculated as,

$$m = \sqrt{2h\left(L + W\right) / k_s WL} \tag{8}$$

Then, the effective two-phase HTC considering fin efficiency, h_{tp}, is evaluated by,

$$h_{tp} = \frac{Q_{latent}}{\left(\sum\left(WL + 2HL\eta_f\right)\left(\overline{T}_{wall} - T_{sat}\right)\right)} \tag{9}$$

where T_{sat} is the saturated temperate of working fluid. The latent heat contributed to boiling heat transfer was derived as,

$$Q_{latent} = P - Q_{loss} - Q_{sensible} \tag{10}$$

Where $Q_{sensible}$ is the sensible heat due to the liquid temperature as follows.

$$Q_{sensible} = GA_c C_p \left(T_o - T_i\right) \tag{11}$$

Significant physical properties of dielectric fluid HFE-7100 are given in [67]. T_{sat} is a function of working pressure (p) in the middle of the microchannel.

The vapor quality was calculated as [116],

$$\chi = \frac{P_{eff} - Q_{sensible}}{\dot{m}h_{fg}} \tag{12}$$

2.3 Uncertainty Analysis

The measurement uncertainties of flow rate, pressure, voltage, current, temperature, and microfabrication resolution are ±0.1%, ±1.5%, ±0.5%, ±0.5%, ±1 ^{o}C, and 3 μm, respectively [118]. Uncertainty propagations are calculated using methods developed by Kline and McClintock [119]. Uncertainties of effective HTC have been estimated to be less than ±2 kW/m^{2}K.

2.4 Flow Boiling Curves

In this study, the flow boiling performance in terms of effective HTC considering all effective heat transfer areas is characterized with mass flux ranging from 462 kg/m^{2}s to 1617 kg/m^{2}s. Figure 2.4 (a) shows that the effective HTCs decrease with the increase in

heat flux. Figure 2.4 (b) shows the overall HTCs based on the heater area as an effective heat flux function. The overall HTCs based on the heating area share almost the same trend with effective HTCs, but ~2 times higher. HTC of ~120 kW/m^{2}K is achieved after the onset of nucleate boiling (ONB) at a mass flux of 1155 kg/m^{2}s. Figure 2.4 also indicates that there are two distinct regimes of HTC curves. For mass flux ranging from 462 kg/m^{2}s to 924 kg/m^{2}s, the curves of HTC become flat after ONB. The sustainable nucleate boiling may contribute to the stable heat transfer rate. At mass flux between 1155 kg/m^{2}s and 1617 kg/m^{2}s, the HTCs gradually decline with the increase in heat flux. The high contribution of convection and the occurrence of the heating surface dryout near the outlet section should be two main reasons for the decrease of HTC, especially near CHF conditions.

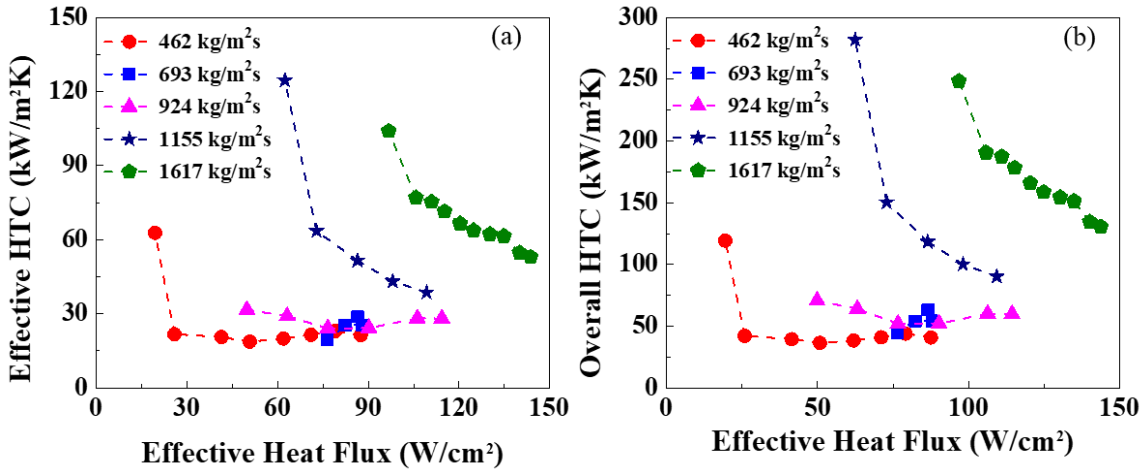

Figure 2.4 (a) Effective HTC as a function of effective heat flux. (b) The overall HTC as a function of effective heat flux.

Moreover, Figure 2.5 present the exit vapor quality in the current configuration remains higher than that from plain wall microchannel and half interconnected channel at the mass velocity of 693 kg/m^{2}s. Mainly, the exit vapor quality at the peak CHF value in the present configuration is 0.92, which is more than twice higher than that in the previous one, indicating a significantly higher portion.

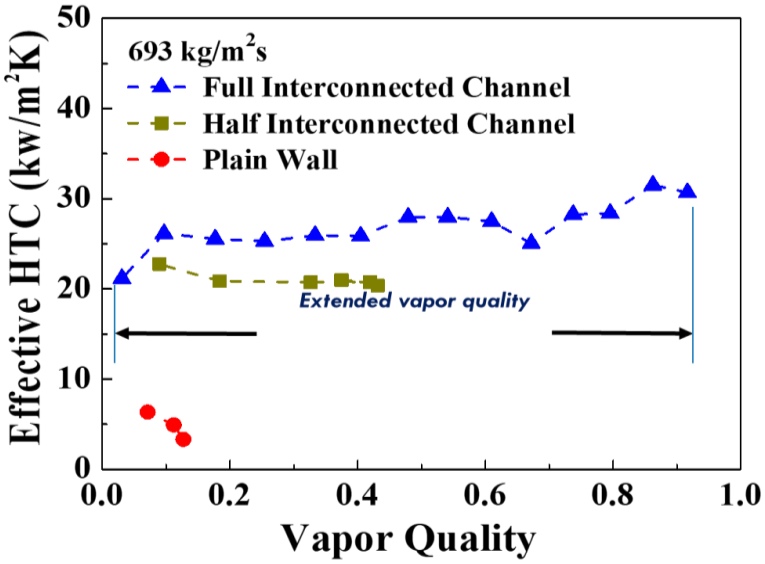

Figure 2.5 Effective HTC as a function of vapor quality.

2.5 New Nucleate Boiling Phenomena and Bubble Dynamics

A complete bubble cycle includes bubble growing time and bubble waiting time, as schematically shown in Figure 2.6. The bubble growing time is the duration from bubble nucleation to departure or collapse on a heating surface. Additionally, the waiting time is when the initiation nucleus on a nucleation site after previous bubble departure or collapse from the same site. The bubble departure frequency can be defined by [120]:

$$f_d = \frac{1}{t_w + t_g} \tag{13}$$

Bubble dynamics in terms of bubble departure diameter (D_d), bubble growth rate ($\frac{dD}{dt}$) the bubble waiting and growth times are characterized and compared with those in plain-wall microchannels at different mass fluxes, as shown in Figure 2.7. Compared to data for plain-wall microchannels, the bubble departure diameter (D_d) and bubble growth rate ($\frac{dD}{dt}$) for the present microchannel configuration are ~2.3 times larger and ~ 3 times faster, respectively, as shown in Figure 2.7 (a, b). As depicted in Figure 2.7 (c, d), bubble

waiting time (t) on the present microchannel configuration is less than half of that on the plain-wall microchannels. The growing time of the present channel is ~ 2.6 times longer than that in plain wall microchannels.

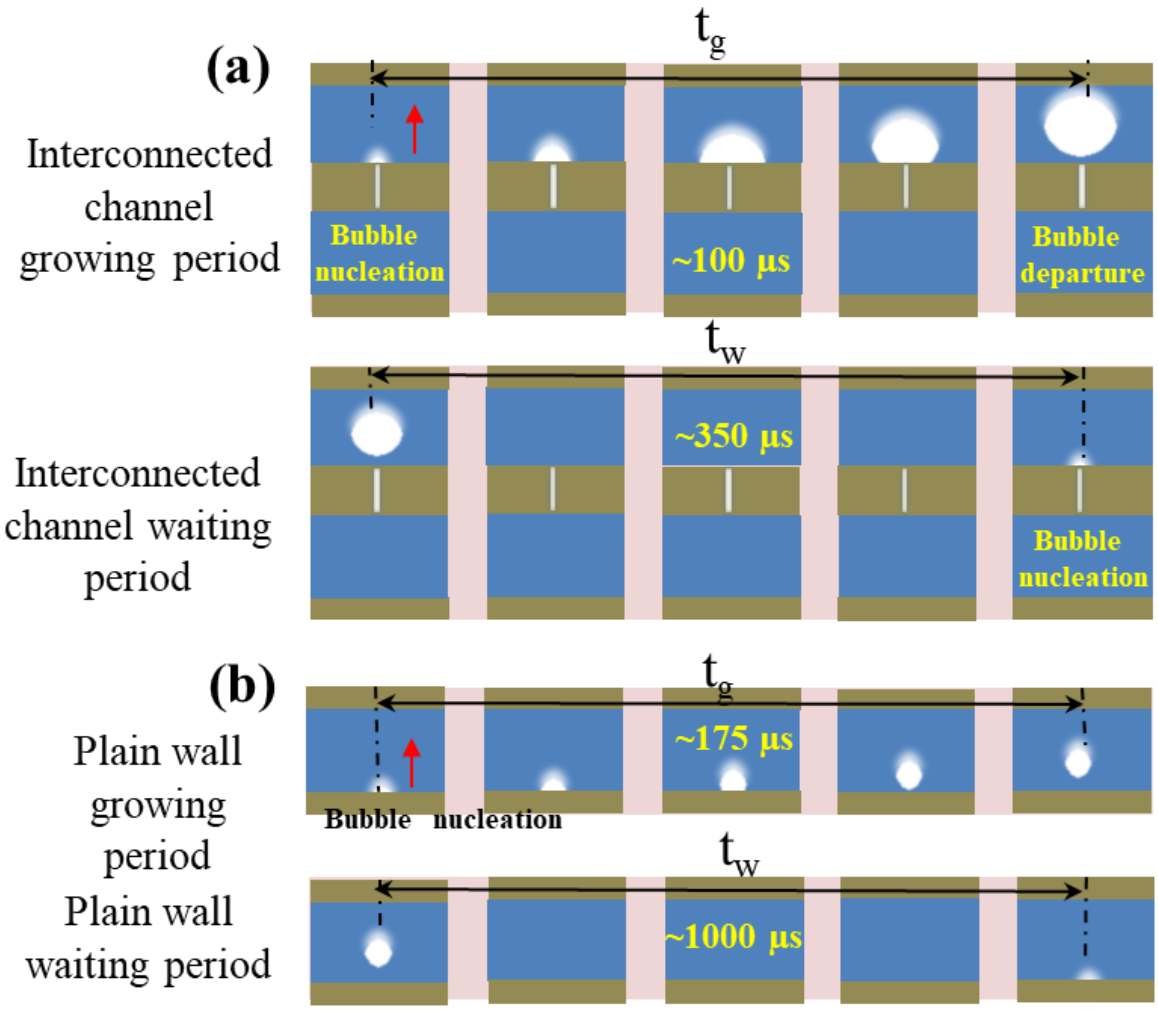

Figure 2.6 Schematic of a bubble growth cycle including waiting and bubble growing periods for (a) interconnected microchannel configuration and (b) plain-wall microchannels.

It would be challenging to meet two requirements for bubble nucleation on a plain wall with highly wetting fluids: residual vapor and superheated fluid. The superior wetting liquid could completely occupy the nucleation sites by removing residual vapor after a bubble departure on the plain wall. Another factor would take a longer time to make the

refilled liquid in the nucleation site to be superheated. These two factors would lead to a significantly longer bubble waiting time. In contrast, in the interconnected microchannels with micro-slots, a small amount of vapor could remain inside the micro-slots after the bubble departure due to the induced capillary pressure. Moreover, the liquid can be quickly sucked into the slots during the bubble departure process and heated up after then, which keeps these micro-slots active continuously and dramatically reduces the bubble growing time, as illustrated in Figure 2.7 (c, d). Visualization has been conducted to validate these two hypotheses and are discussed in the next section.

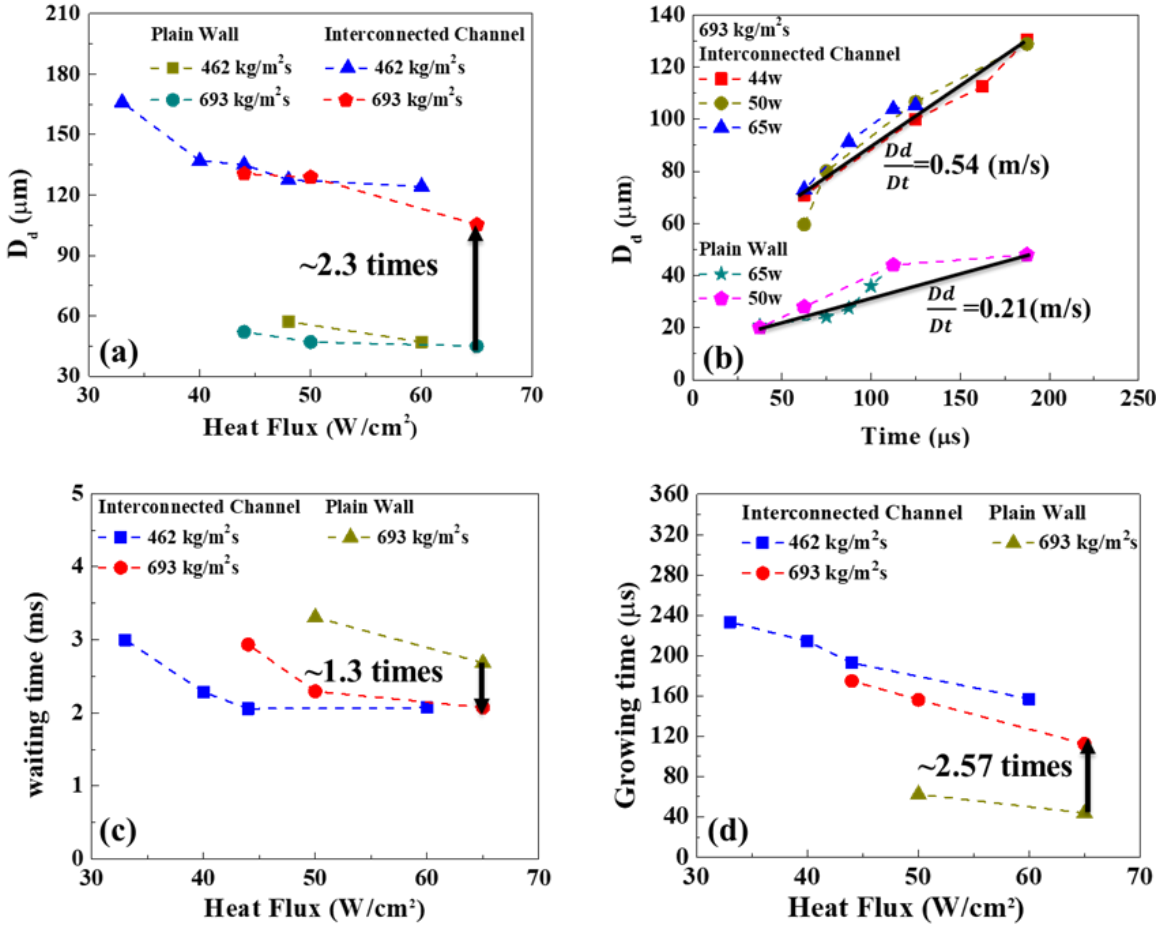

Figure 2.7 Comparisons of bubble dynamics between the present design and plain-wall microchannels at a mass flux of 693 kg/m^{2}s. (a) Bubble departure diameter (D_d) as a function of heat flux, (b) bubble diameter as a function of time, and (c) the bubble waiting time as a function of heat flux. (d) bubble growing time as a function of heat flux.

Figure 2.8 shows three sequential frames of liquid jetting from the micro-slots. These images are selected from image sequences at a sample rate of 7,000 frames per second (fps). The observed liquid jetting should be pumped out by pressure imbalance between the neighboring channels owing to unstable non-uniform distributions of two-phase flow [30]. More importantly, this jetting flow well validates residual vapor and liquid inside the slots, significantly shortening the bubble growing time.

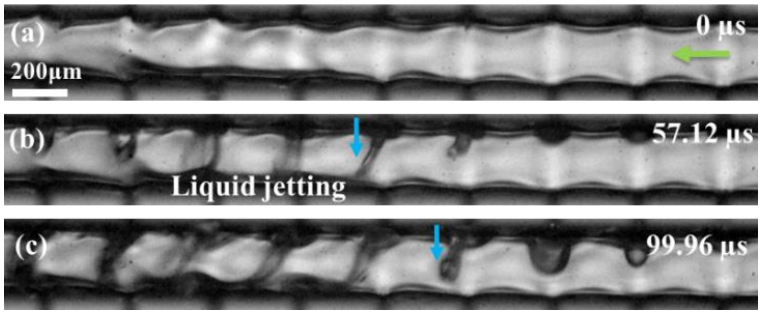

Figure 2.8 Liquid jetting from these slots at 40W/cm^2 and mass flux of 462 kg/m^{2}s. (a) initial stage of non-fluid jetting status. (b, c) fluid jetting observed in two sequential images.

For comparison, Figure 2.9 depicts the waiting period of nucleate boiling in plain-wall microchannels at a mass flux of 693 kg/m^{2}s and a heat flux of 65 W/cm^2. The bubble departure frequency in the plain-wall microchannels is ~ 355 Hz, as shown in Figure 2.12 (a), lower than ~ 452 Hz at similar working loads of interconnected channels. The bubble departure diameter is ~45 μm, around 2.3 times smaller. The waiting time for plain wall microchannel is ~1.3 times longer than that in interconnected microchannels, as shown in Figure 2.7 (a) and (c). Figure 2.9 (a) and (d) clearly show that bubble nucleation of the plain wall randomly occurs. The bubble departure frequency in the plain wall microchannels is much lower than that of the present microchannels, the shorter bubble waiting time.

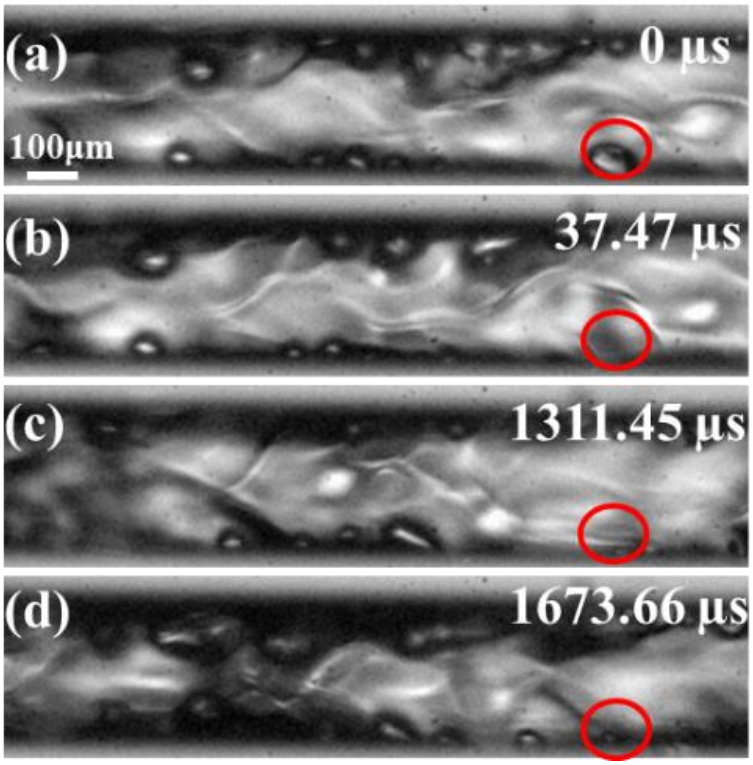

Figure 2.9 Waiting time in plain wall microchannels at a mass flux of 693 kg/m^{2}s and a heat flux of 65 W/cm^2. (a) Bubble departs from the wall surface, (b, c) no bubble nucleation appears with a long waiting period, and (d) new bubble appears at same nucleation site.

Figure 2.10 shows the bubble growth process in the interconnected microchannels at mass flux of 462 kg/m^{2}s and heat flux of 40 W/cm^2. Compared to the plain-wall microchannel, the bubble growth and departure or collapse in the interconnected channel has been well coordinated. The bubble growing time is measured at ~ 220 μs, as shown in Figure 2.7 (d).

Active nucleation site density is another parameter to characterize the bubble dynamics. The active nucleation site density was estimated by dividing the measured number of active nucleation sites by the total area using images captured by a high-speed camera . As shown in Figure 2.11, the active nucleation site density of interconnected microchannels is a constant of 2240 sites/cm^2 owing to the 100% active nucleating sites,

which is ~ 1.86 times higher than the cavity structure at a similar working condition of a mass flux 693 kg/m^{2}s and ~ 1.7 times higher than that of plain-wall microchannels.

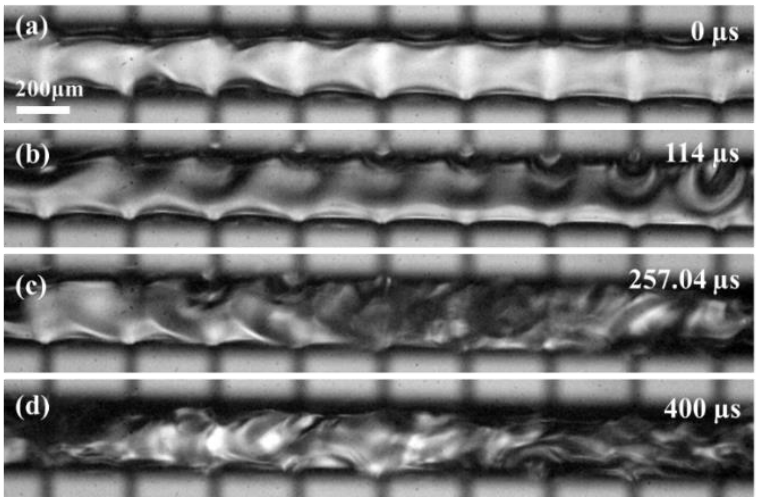

Figure 2.10 A bubble growth process at a mass flux of 462 kg/m^{2}s and a heat flux of 40W/cm^2. (a) The initial stage for the interconnected channel, (b) bubble growing from micro-slots, (c) bubble collapsing or departing from the channel, and (d) bubble merging.

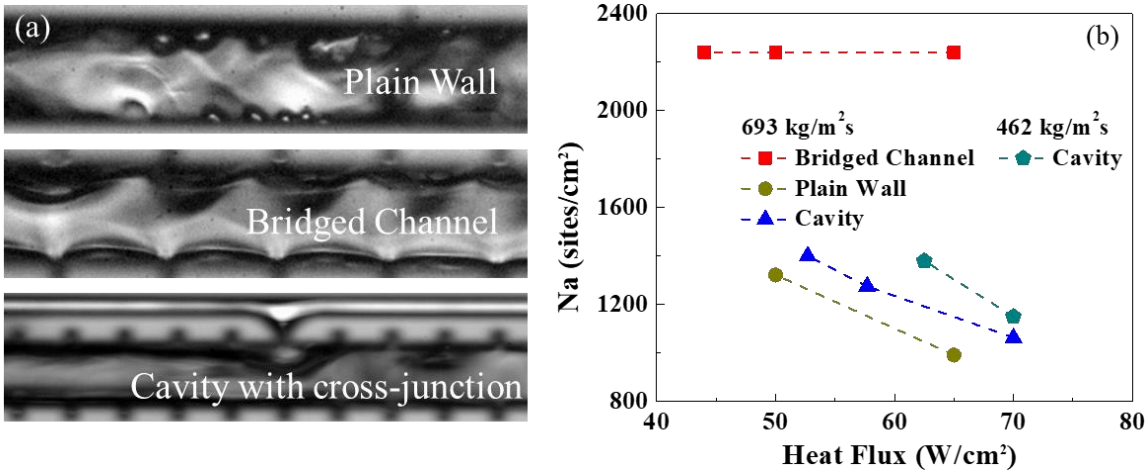

Figure 2.11 (a) Designs of different configurations. (b) Active nucleation site density as a function of heat flux with different configurations.

The micro-slots in the interconnected channels were 100% activated during the boiling, but reentry-cavities in our previous design were only 22.2% activated according

to experiment data [67]. High active nucleation site density can facilitate nucleate boiling of heat transfer rate.

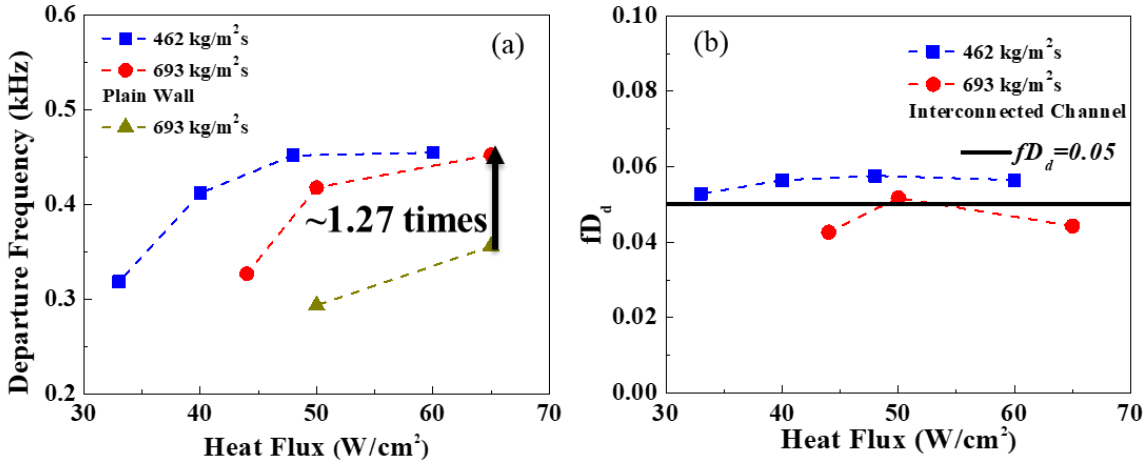

Figure 2.12 (a) Bubble departure diameter increases with the increase of heat flux at different mass fluxes. (b) $f \cdot D_d$ as a function of heat flux.

Figure 2.12 (a) shows the effects of mass flux and heat flux on bubble departure frequency, which increases with the enhancement of heat flux and decreases the increase of mass flux on the present microchannel configuration. In additional. Figure 2.14 (c) demonstrates that the switching frequency increases as the heat flux increases at different mass fluxes. The trends of bubble switch frequency were nearly overlapped in two different mass fluxes, meaning that it should be primarily determined by nucleate boiling. Bubble departure frequency and departure diameter are highly affected by the superheat. A reported study has suggested the bubble departure diameter is closely related to departure frequency in the form of $f \cdot D_d$=constant [121]. In this study, a fit curve is $f \cdot D_d = 0.05$. It is obtained from curve-fitting experimental results in Figure 2.12 (b).

2.6 Coordinated Nucleate Boiling

In conventional microchannels, nucleate boiling in an individual channel is usually isolated. It is highly desirable to harmonically coordinate these usually isolated boiling

processes to enhance nucleate boiling. On the present microchannel configuration, bubble nucleation switches between two sides of each wall at a high frequency.

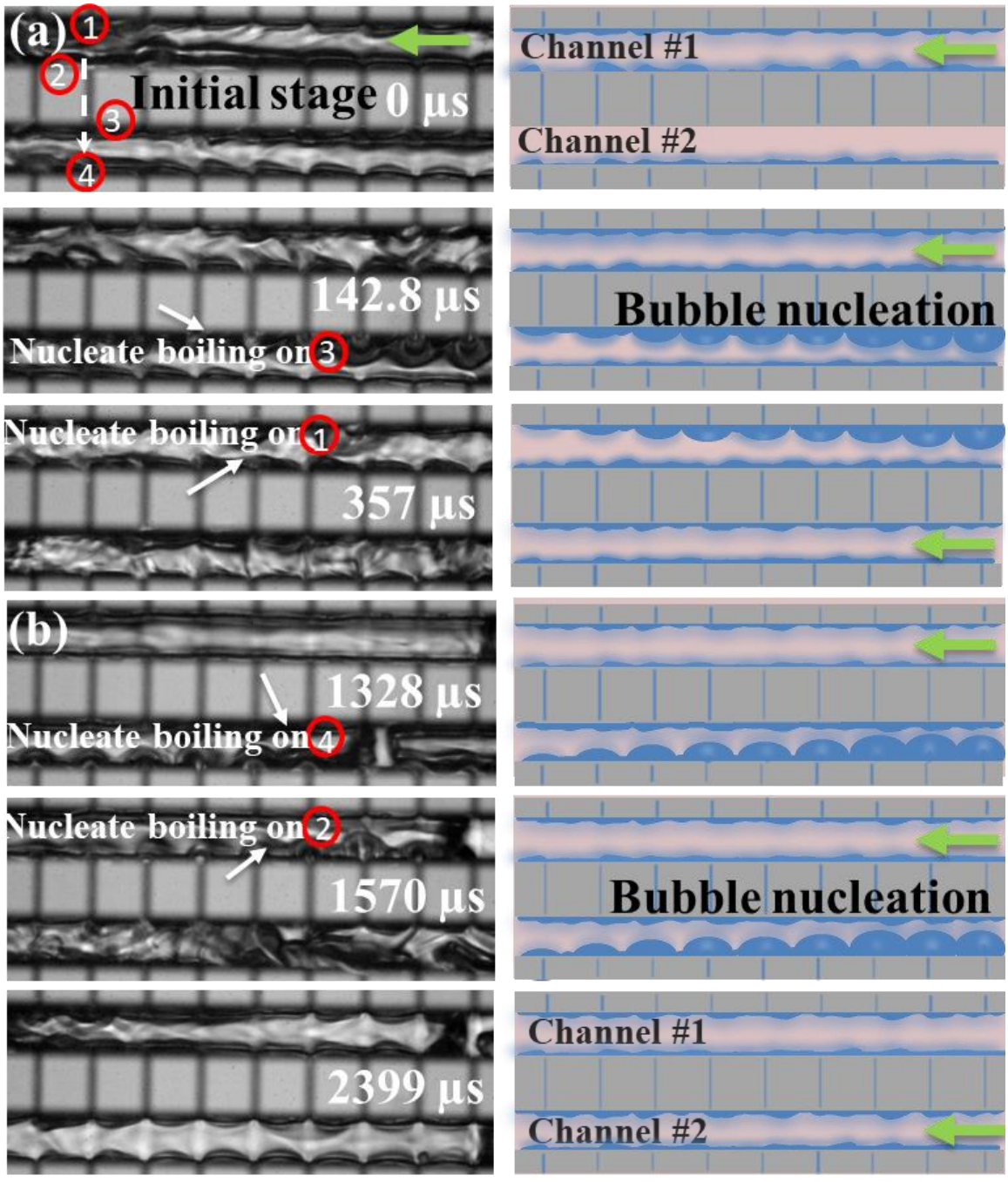

Figure 2.13 (a, b) A top-view of the highly coordinated and rapid nucleate boiling at 2597 Hz switching frequency of nucleate boiling between the two sides of a microchannel at a heat flux of 40W/cm^2 mass flux of 462 kg/m^{2}s. Nucleate boiling occurred from both sides of the channel wall sequent.

More importantly, the bubble nucleation and departure process on one side of the wall greatly enhances bubble nucleation through shorting bubble waiting time. Thus, nucleate boiling has been well-coordinated through these well-designated micro-slots, as illustrated in Figure 2.13 (a).

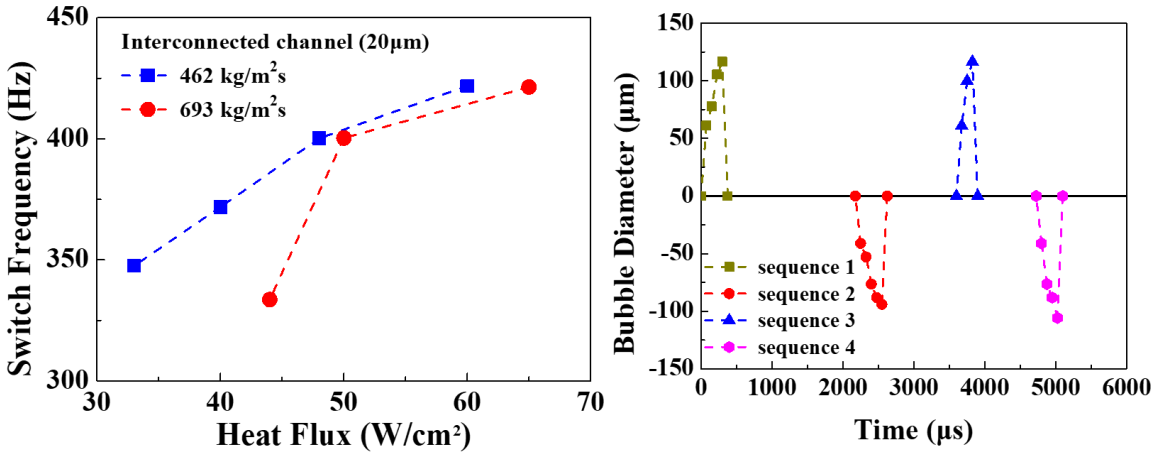

Figure 2.14 (a) Bubble diameter as a function of time. (b) Nucleate boiling switching frequency as a function of heat flux.

Figure 2.13 (a) has shown the new nucleate boiling phenomena in the middle section of the interconnected microchannels at a mass flux of 462 kg/m^{2}s and a heat flux of 40 W/cm^2. The bubble departure frequency is ~ 411 Hz with a departure diameter of ~152 μm. The concept clearly shows the process of bubble growth, collapse or departure, and switching between two neighboring channels. The bubble first appears on the upper surface of channel three, and after the bubble collapse or departure, bubbles nucleate and grow on the top surface of channel one. The same situation occurs at the bottom surface of channels two and four after the bubble departs from channel three, as shown in Figure 2.13 (a). The details about the bubble diameter variation with the time change have shown in Figure 2.7 (b). It is indicated that the diameter of bubble growth, collapse, and the waiting periods for the next pulse is almost systematic patterns.

2.7 Enhanced HTC

The switching period in this study, as shown in Figure 2.14, is defined as a period from bubble growth to departure or collapse on one side of the wall until the initial nucleus appears at the nucleation cavities on the other side of the wall. The whole process has been illustrated in Figure 2.13 (a), from wall two to wall three or from wall three to wall two, according to the equation $f=1/t_s$.

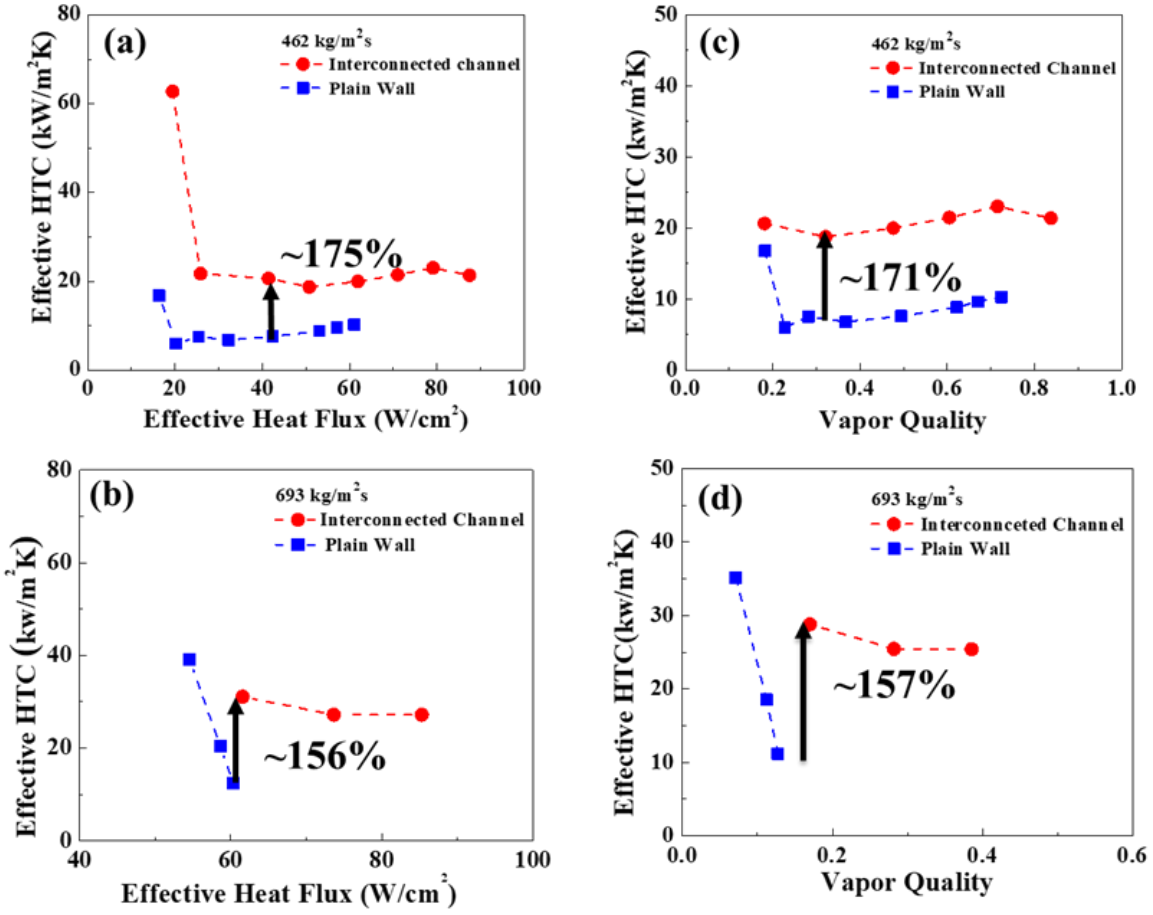

Figure 2.15 Significant enhancements of HTC are achieved on the present design compared to plain wall microchannels. (a, b) Effective HTC as a function of effective heat flux. (c, d) Effective HTC as a function of vapor quality.

Compared to the plain-wall microchannel configuration, effective HTCs considering all effective heat transfer areas in this study are substantially enhanced, as shown in Figure 2.15 (a, b). Significant enhancements of ~175% and ~156% are achieved,

respectively, at the mass flux of 462 kg/m^{2}s and 693 kg/m^{2}s, as shown in Figure 2.15 (a, b). The enhanced mechanism of HTC is explored as follows. On the plain wall surface, it is difficult to form large thin liquid film areas due to the low surface tension of HFE-7100. The explosive boiling would possibly take place and blow off the liquid film from the heating surface, resulting in local dryout spots. Meanwhile, the suppressed nucleate boiling due to the highly rewetting ability of HFE-7100 would deteriorate heat transfer rates.

The interconnected microchannel configuration developed in this study can overcome these challenges, as mentioned above. Nucleate boiling has been drastically enhanced by increasing active nucleation site density and bubble growth rates. The 28 micro-slots can serve as nucleation sites to greatly enhance nucleate boiling. More importantly, highly desirable periodic rewetting is enabled in each channel and coordinated between these micro-slots channels.

The comparison between the current design and the plain-wall microchannels at different mass fluxes was conducted, as shown in Figure 2.15. Two types of effects, including heat flux and vapor quality, were compared to indicate the heat transfer mechanism, as shown in Figure 2.15 (c, d). The interconnected channels can enable significantly higher vapor quality (enhanced up to ~ 186% at a mass flux of 462 kg/m^2·s) than the plain wall microchannels do. This is because the new microchannel configuration increases high nucleation-site-density and keeps them activated, enhancing latent heat transfer contributions as indicated by high exit vapor quality. Note that HTC remains stable as a function of the vapor quality.

$$q''_{advection} = q''_{total} - q''_{nuc} - q''_{eva} \tag{14}$$

During the coordinated nucleate boiling process, heat is primarily transferred by advection, nucleate boiling, and evaporation. To better understand the enhanced mechanisms, these three heat transfer modes have been analyzed. The advection heat flux Eq. (14) including mixing and convection contributions, which results from the disruption of the thermal boundary layer during bubble growth, lift-off, or collapse [122]. The periodic disruption of the thermal boundary layer can reduce thermal resistance [123-127]. The nucleate boiling heat flux Eq. (15) is defined as the amount of heat carried away by these bubbles nucleated on the heating surface. In the present microchannel configuration, the whole growth process of each bubble can be accurately measured by high spatiotemporal images captured by a high-speed camera (Phantom v7.3) due to the large bubble departure size, extended growth time, and fully activated sites as illustrated in Figure 2.7. The evaporation heat flux can be estimated by excluding nucleate boiling from the total latent heat flux Eq (16).

$$q''_{nuc} = \rho_v \cdot h_{fg} \cdot V_b \cdot Na \cdot f \tag{15}$$

$$q''_{eva} = \frac{\chi \cdot m \cdot h_{fg}}{A_{heater}} - q''_{nuc} \tag{16}$$

Figure 2.16 summarizes the ratio of three major heat transfer mode contributions to the total effective heat flux at different mass fluxes between the two configurations. In the plain wall microchannels, the advection heat transfer at a mass flux of 693 kg/m^{2}s dominates heat transfer. The heat transferred by nucleate boiling and evaporation only accounts for a small fraction.

Figure 2.16 (a, b, c) shows that the nucleate boiling contributes 20% to 40% of the total heat transfer rate in the overall heat transfer process. Simultaneously, evaporation accounts for 21%-46% of total heat removal, more than doubled compared to these in plain-wall microchannels.

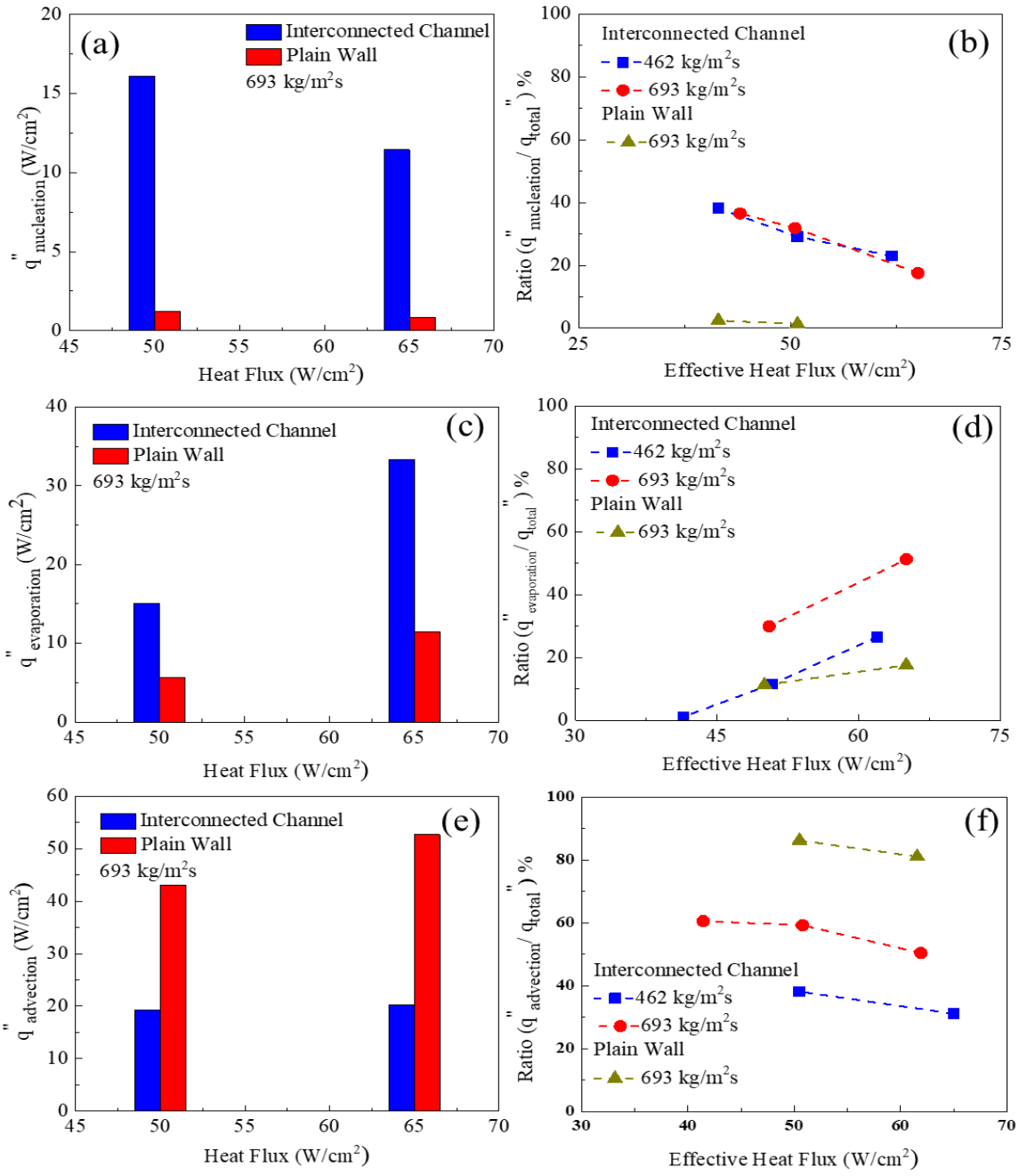

Figure 2.16 Comparison of proportional energy. (a) Bar graph of nucleation heat flux. (b) Bar graph of evaporation heat flux. (c) Bar graph of advection heat flux. (d) Nucleation

heat flux ratio as a function of effective heat flux. (e) Evaporation heat flux ratio as a function of effective heat flux. (f) Advection heat flux ratio as a function of effective heat flux.

In those testing conditions as shown in Figure 2.16, the latent heat contribution has been substantially enhanced, which should be the primary reason behind the drastically enhanced HTCs enabled by the present microchannel configuration.

2.8 Enhanced CHF with the Reduced Pressure Drop

Figure 2.17 compares the enhanced CHF at different mass flux ranging from 462 kg/m^{2}s to 1617 kg/m^{2}s in the present design with the plain wall microchannels. A significant enhancement of ~76% has been achieved at mass flux of 1155 kg/m^{2}s by enhancing liquid rewetting through the micro-slots. Moreover, a slight decrease of ~6% of two-phase pressure drop was found compared to the plain-wall microchannels, as shows in Figure 2.17 (b). The enhancement of CHF indicates that micro-slots play a vital role in enhancing CHF. The rapid and periodic rewetting enabled by the highly coordinated nucleate boiling in neighboring channels is the main factor leading to the enhanced CHF.

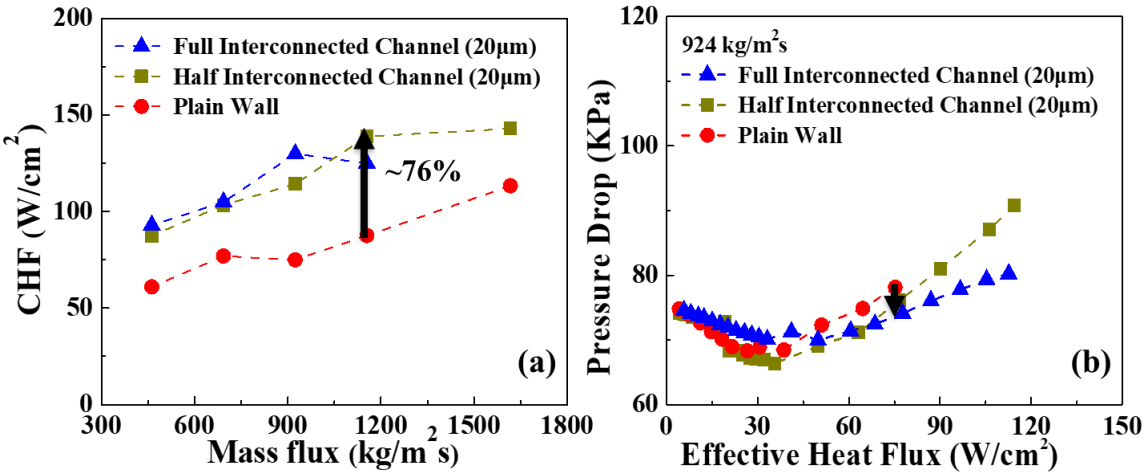

Figure 2.17 Comparison of (a) CHF and (b) two-phase pressure drop between the present design and plain wall configuration.

Usually, premature CHF conditions can be triggered by explosive boiling, flow instabilities, and partial dryout. For plain-wall microchannels with IRs, when heat flux increases, explosive boiling is likely to occur because of superheated HFE-7100 due to its low thermal conductivity. Then, the thin liquid film would be expelled away from walls, and eventually, the vapor layer forms on the heating surface near inlet regions. The integration of micro-slots has successfully prevented the occurrence of explosive boiling.

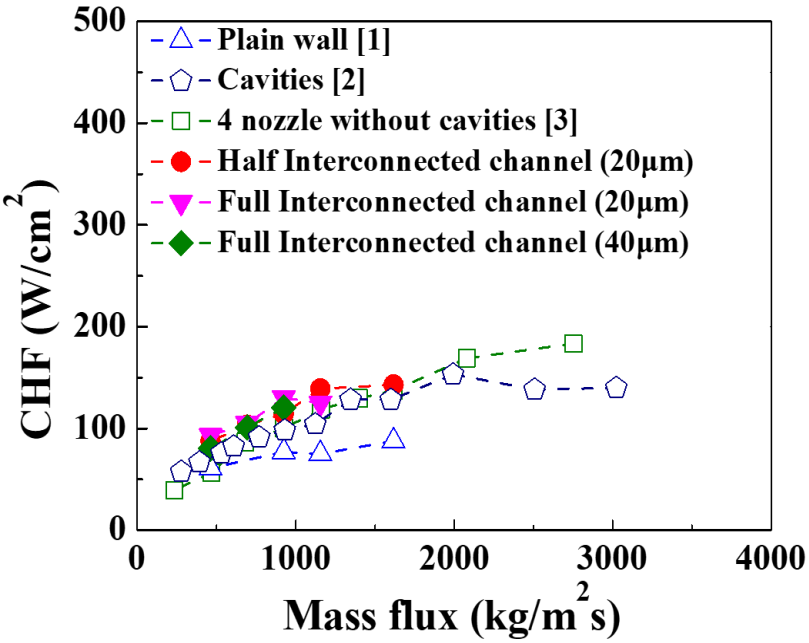

Figure 2.18 Comparison of CHF with different microchannel configurations.

The heating surface dries out because low rewetting capability is one of the main factors resulting in premature CHF conditions. Enhanced liquid spreading is essential to increase CHF. Normally, surface rewetting is highly influenced by working fluid properties, surface conditions of heating surfaces, and two-phase transport regimes. However, it is challenging to increase CHF on highly wetting HFE-7100. In conventional plain-wall microchannels, it is difficult to maintain liquid film on the heating surface on HFE-7100 because of its low surface tension. The potential solution of this issue is to

enhance capillary pressure through surface modification, such as nanowires, to compensate for the low surface tension. Although local rewetting is enhanced in microchannel covered with nanowires, the global liquid supply greatly suffers from high flow resistance resulting from dense nanowires. As a result, the enhancement of CHF is not significant using nanowires. In this study, individual microchannel interconnected by micro-slots would greatly promote liquid rewetting.

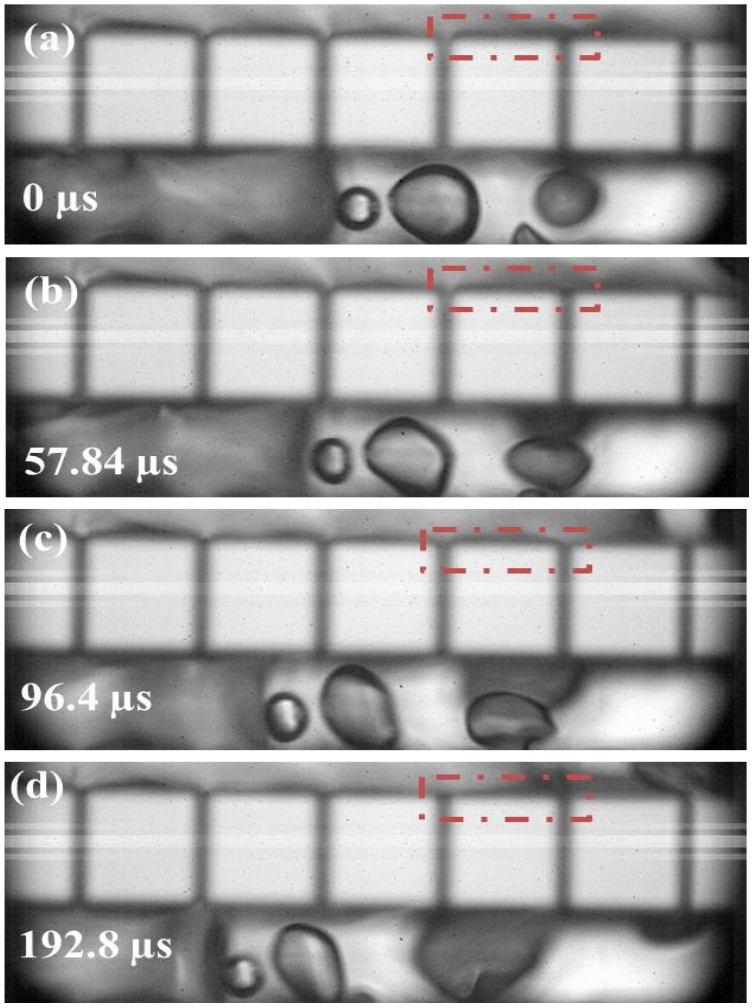

Figure 2.19 Thin liquid film can be inhaled in micro-slots when the bubble grows in the present study at a mass flux of 462 kg/m^{2}s and a heat flux of 44 W/cm^2.

Figure 2.19 shows that thin liquid film can be sustained between the micro-slots, effectively delaying local surface dryout at mass flux of 462 kg/m^{2}s and heat flux of 44 W/cm^2 in the present study. The high-frequency nucleation boiling in the present design can also improve liquid supply to the neighboring channels.

Figure 2.18 shows the early result of CHF on a highly wetting dielectric fluid of HFE-7100. The trend of CHF indicates that this new design of interconnected microchannel performs better heat transfer performance. The micro-slots served as reentry cavities extremely enhanced the rewetting ability and delayed local dryout, leading to higher CHF performance. However, to obtain more persuasive results, more experimental data should be accomplished with interconnected microchannels to study the enhanced mechanism of the present design with HFE-7100 as working fluid.

2.9 Conclusions

In this study, flow boiling of HFE-7100 has been systematically characterized by an innovative microchannel configuration. Rapid and sustainable nucleate boiling has been well-coordinated through designated micro-slots for the first time. Compared to the plain wall microchannels, HTC and CHF have been considerably enhanced without compromising two-phase pressure drop. The primary HTC enhancement mechanism is the higher contribution of latent heat transfer on the present microchannel configuration. The highly coordinated and high frequency nucleate boiling process also greatly delays CHF conditions. The bubble dynamics have been systematically characterized in terms of bubble growth rates, bubble departure diameter, and bubble departure frequency and the enhanced nucleate boiling is discussed as well.

CHAPTER 3 EFFECTS OF SIZE AND NUMBERS OF MICRO-SLOTS

In this study, microchannels with three different sizes of micro-slots are used to elucidate the effectiveness of different sizes and numbers of micro-slots in interconnected microchannels on flow boiling heat transfer. The new configuration is developed based on the experimental and theoretical study of half interconnected microchannel design [128]. With the improved configurations, nucleate boiling can be further enhanced, and the active nucleation site density can be extended to the entire channel.

In additional, based on the improved microchannel configuration, the enhancements of CHF and HTC are not at the penalty of pressure drop. The high-frequency rewetting with micro slots can significantly improve liquid supply to the neighboring channels. The transient state features for the present improved microchannel configuration proved that the real-time wall temperature of the present design fluctuates periodically and more stable than the chaotic temperature fluctuation of plain wall microchannel, which shows that micro slots can effectively manage the boiling instability.

3.1 Design of Device Architecture

An innovative microchannel configuration has been fabricated on a 500μm silicon wafer with five main microchannels which the dimensions of length × width × depth is 10mm × 200μm × 250μm. In this design, all five parallel microchannels are interconnected fully by micro-slots on each intermediate wall, as shown in Figure 3.1. To achieve more effective results, these micro-slots were designed with three different sizes (10μm, 20μm,

40μm) for each full interconnected channel separately as nucleation sites to enhance and sustain nucleate boiling to enhance the HTC and CHF compare to the previous study of half interconnected channel and plain wall microchannels.

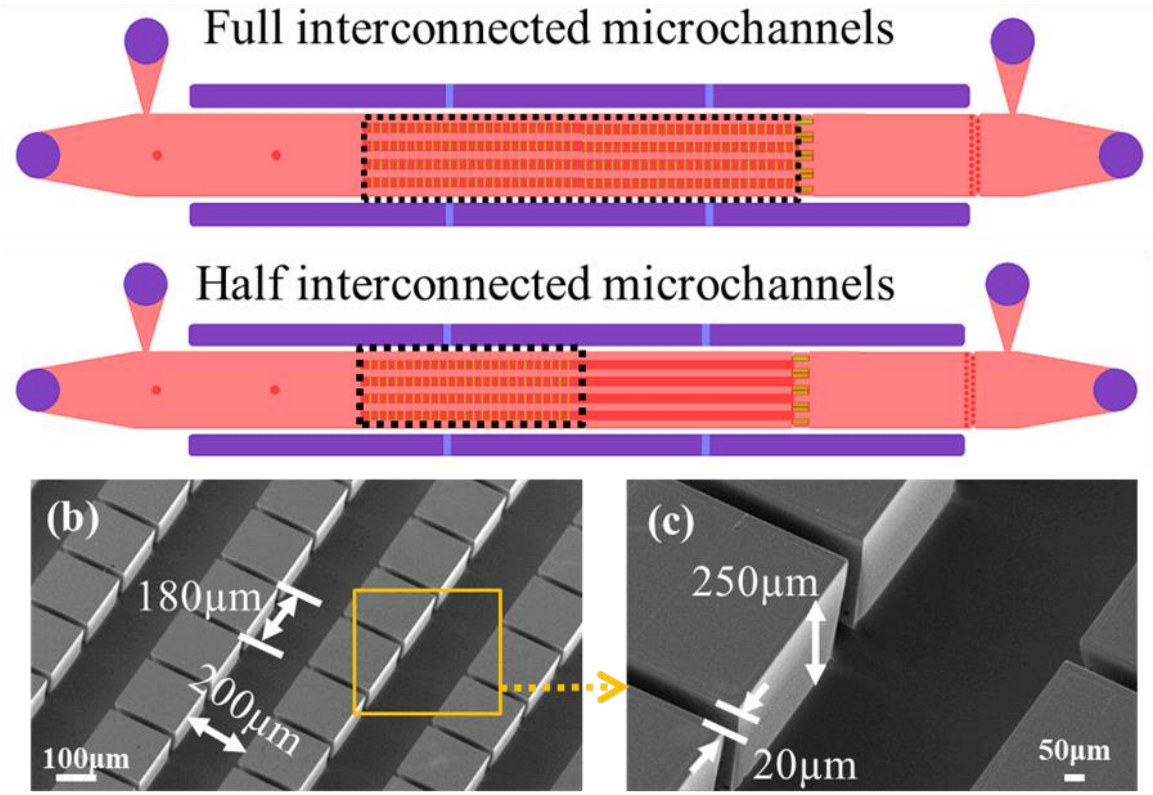

Figure 3.1 (a) The concept of full & half interconnected channels. (b) The top view of the SEM image of the full interconnected channel structure with the dimension of wide and length. (c) The side view of SEM image with dimension of micro-slots and microchannel wall height.

An aluminum film resistor (10mm×2mm×1.2μm) was deposited on the backside of the microchip to supply uniform heat flux and served as a thermistor to measure wall temperature. A 500μm thick Pyrex glass wafer was bonded to the silicon substrate to seal the channels and form a visualization window. HFE-7100 at room temperature has been used as a working fluid. More importantly, nucleate boiling in neighboring microchannels can be harmonically coordinated for the first time, leading to significantly higher bubble

growth rates and rewetting frequency, and significantly better heat transfer performance. The studies above have presented further detail of the fabrication process and experimental detail [128, 129].

3.2 Data Reduction

In experiments, the input power was calculated by multiplying the DC voltage (V) with current (I). Then the effective heat flux was calculated after subtracting the heat loss, Q_{loss}, (pre-calibrated between the ambient environment and the test device) from the total input power, P, as follow,

$$q''_{eff} = \frac{P - Q_{loss}}{A} \tag{17}$$

Where A is the base heating area. Based on the pre-calibrated linear relationship between temperature and electrical resistance, the average temperature of the microheater (on the backside of the device) was calculated as,

$$\bar{T}_{heater} = K\left(R - R_a\right) + T_a \tag{18}$$

R_a is the resistance of the microheater at ambient temperature T_a, and K is the slope of pre-calibration. The average temperature at the bottom wall of microchannels was then derived as,

$$\bar{T}_{wall} = \bar{T}_{heater} - \frac{q''_{eff}\delta}{k_s} \tag{19}$$

Where δ and k_s are the substrate thickness, the thermal conductivity of silicon, respectively.

The fin efficiency, η_f, of a finite fin was estimated from

$$\eta_f = \frac{\tanh(mH)}{mH} \tag{20}$$

The equation of η_f is used to characterize fin performance and to calculate the average effective HTC, where the parameter m was calculated as,

$$m = \sqrt{2h\left(L+W\right)/k_s WL} \tag{21}$$

Then, the effective two-phase HTC considering fin efficiency, h_{tp}, is evaluated by,

$$h_{tp} = \frac{Q_{latent}}{\left(\sum\left(WL + 2HL\eta_f\right)\left(\bar{T}_{wall} - T_{sat}\right)\right)} \tag{22}$$

Where T_{sat} is the saturated temperate of working fluid. The latent heat contributed to boiling heat transfer was derived as,

$$Q_{latent} = P - Q_{loss} - Q_{sensible} \tag{23}$$

Where $Q_{sensible}$ is the sensible heat due to the liquid temperature as follows.

$$Q_{sensible} = GA_c C_p \left(T_o - T_i\right) \tag{24}$$

Major physical properties of dielectric fluid HFE-7100 are given in [67]. T_{sat} is a function of working pressure (p) in the middle of a microchannel.

The vapor quality was calculated as [116],

$$\chi = \frac{P_{eff} - Q_{sensible}}{\dot{m}h_{fg}} \tag{25}$$

3.3 Uncertainty Analysis

The measurement uncertainties of flow rate, pressure, voltage, current, temperature, and microfabrication resolution are ±0.1%, ±1.5%, ±0.5%, ±0.5%, ±1 ^{o}C, and 3 μm, respectively [118]. Uncertainty propagations are calculated using methods developed by Kline and McClintock [119]. Uncertainties of effective HTC have been estimated to be less than ±2 kW/m^{2}K.

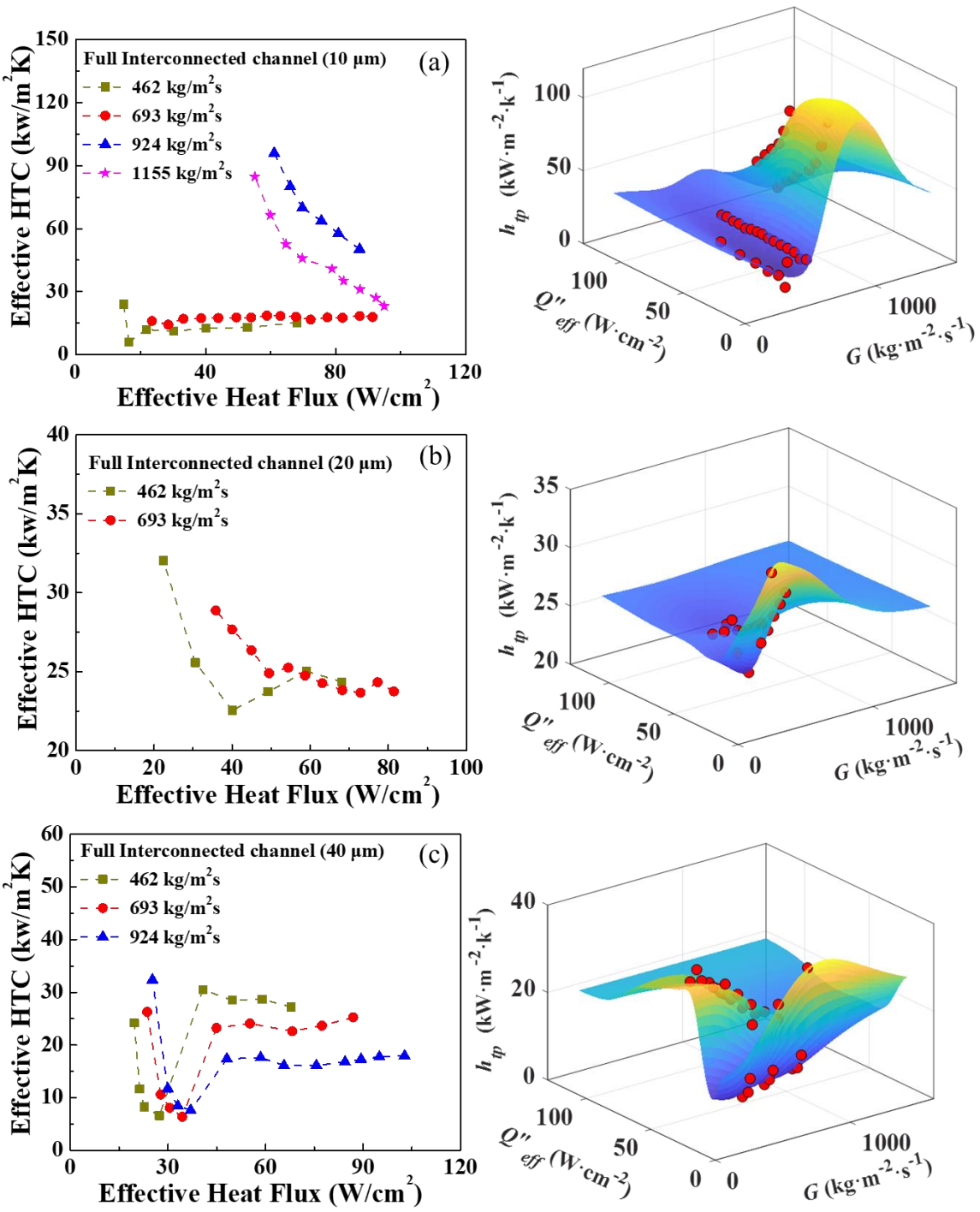

Figure 3.2 Significant enhancements of HTC are achieved on the present design with smaller micro-slots size. (a) Effective HTC as a function of effective heat flux at micro-slots size 10μm. (b) Effective HTC as a function of effective heat flux at micro-slots size 20μm. (c) Effective HTC as a function of effective heat flux at micro-slots size 40μm. (d), (e), (f) Data regression for mass flux and effective heat flux.

3.4 Flow Boiling Curves

In this study, three micro-slots with different sizes are designed to examine the different heat transfer performance in various mass fluxes. As Figure 3.2 (a) shows, the effective HTC as a function of effective heat flux different mass flux with the micro-slots size of 10μm, at a mass flux of 924 kg/m^{2}s the effective HTC achieved an extremely high value compared to the other flow conditions, however, as the mass flux increase, the HTC trend line became decrease although it still has a larger enhancement contrast with the results for 462 kg/m^{2}s and 693 kg/m^{2}s. Figure 3.2 (b, c) demonstrates that increasing micro-slots size leads to worse heat transfer performance as the mass flux rises. As Figure 3.2 (c) indicates before ONB, the HTC has a small growth rate as the mass flux increases. The ONB HTC at mass flux of 462 kg/m^{2}s enhances ~100% compared with the 924 kg/m^{2}s flow condition. The main reason that causes this phenomenon is that the larger slots size causes the high contribution of convection and the heating surface dryout near the outlet section and eventually decreases the HTC.

Figure 3.2 (a, b, c) also indicates the data regression for mass flux and effective heat flux. An optimization study was established using the MATLAB program from the data acquired from previous experimental results collected by LabView. As Figure 3.2 (a) shown, at the microchannel with 10μm micro-slots size, the optimal result can be acquired at the mass flux of 1015 kg/m^{2}s. And Figure 3.2 (b) indicated that at the microchannel with 20μm micro-slots size, the optimal result is at the mass flux of 669 kg/m^{2}s. The mass flux of 294 kg/m^{2}s is the optimal result of the microchannel with 40μm micro-slots size based on the aforementioned experimental data. More optimization studies would be developed in future work.

3.5 Enhanced Nucleation Boiling and CHF

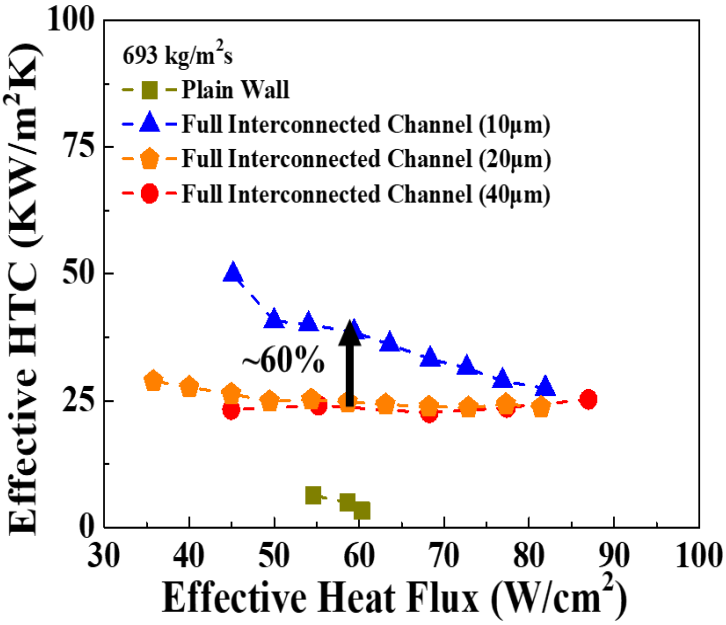

Figure 3.3 Effective HTC as a function of heat flux with three micro-slots sizes.

Figure 3.3 shows the heat transfer performance with the different micro-slots size microchannels at the same mass flux of 693 kg/m^{2}s. An enhancement of ~ 12.7 times is achieved in the present microchannels with 10μm compared to plain wall microchannels at mass flux of 693 kg/m^{2}s, although the micro-slots with size of 20μm and 40μm have almost the same trend. The effective HTC of the full interconnected channel with 10μm slightly decreases. The effective HTC for the 20μm and 40μm configurations is nearly invariable and increases heat flux.

As Figure 3.4 indicated, compared with half interconnected channel and plain wall microchannel, present design with full interconnected channel significantly improved effective HTC up to 345% at mass flux of 462 kg/m^{2}s and 693 kg/m^{2}s. Figure 3.4 shows that the curve of the full interconnected channel at the mass flux of 462 kg/m^{2}s has a steep offset as the effective heat flux reached 60 W/cm^2. The high contribution of convection

and the occurrence of the heating surface dryout near the outlet section should be two main reasons for the decrease of HTC, especially near CHF conditions.

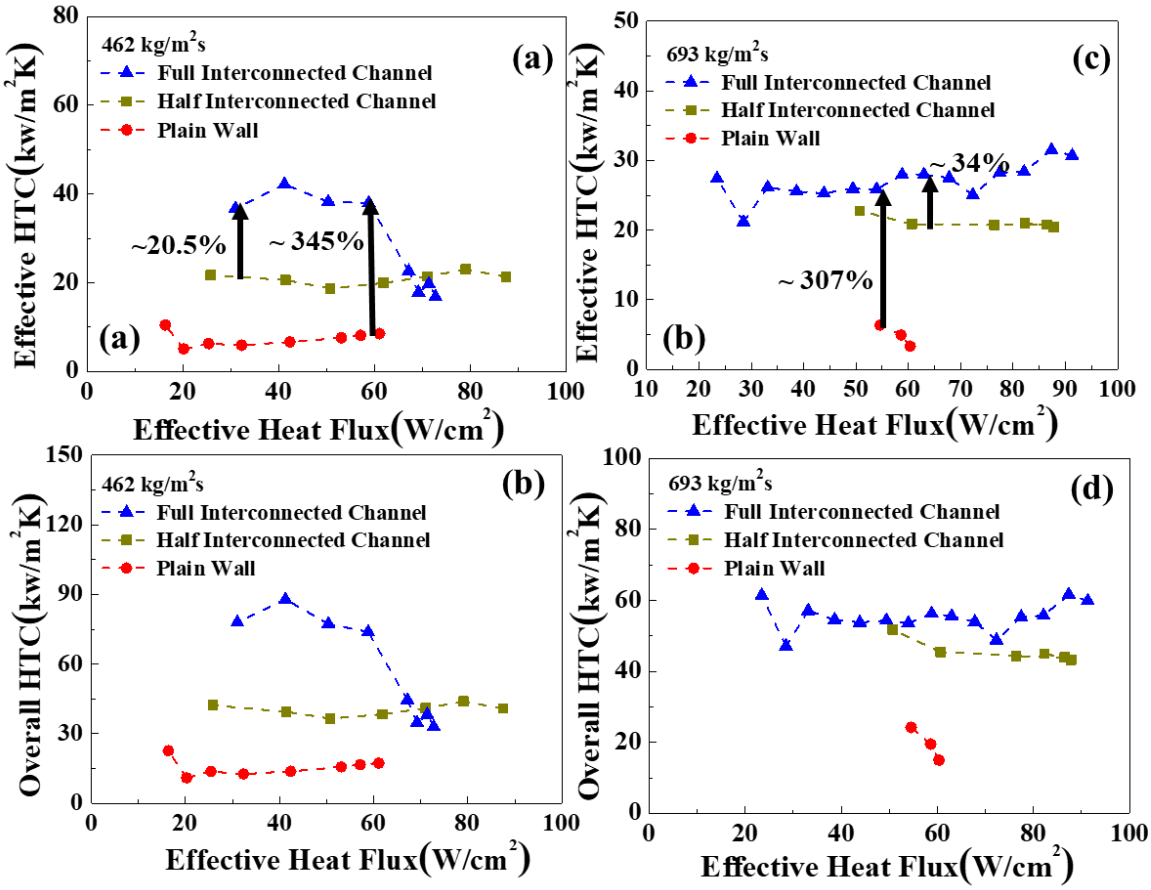

Figure 3.4 Effective HTC as a function of effective heat flux and overall HTC as a function of heat flux at the mass flux of 462 kg/m^{2}s and 693 kg/m^{2}s.

According to the results in half interconnected channel configuration and plain wall microchannel configuration as a baseline, Figure 3.4 (a) indicates that the full interconnected microchannel has higher effective HTC at low heat flux than the other two structures. However, the trend line has a sudden decrease as the effective heat flux reached 60 W/cm^2. Besides, the enhancement of the HTC has a peak value of 43 kW/m^{2}K, which is ~ 345% higher than the plain wall microchannel and ~ 21.5% larger than the half interconnected microchannel. Figure 3.4 (b) shows the overall HTCs based on the heater

area as a function of effective heat flux. The overall HTCs based on the heating area share almost the same trend with effective HTCs, but ~2 times larger. Figure 3.4 also demonstrates that at mass flux of 462 kg/m^{2}s, the curves of effective HTC of half interconnected microchannel and plain wall microchannel become flat after ONB. Nevertheless, the trend of full interconnected microchannels has a sudden drop. The high contribution of convection and the occurrence of the heating surface dryout near the outlet section should be two main reasons for the decrease of HTC, especially near CHF conditions.

To deeply understand the heat transfer capability of the present microchannels, Figure 3.5 summarizes the major enhancement results in this study. The delayed boiling incipience deteriorates the heat transfer performance, as shown in Figure 3.5(a). The slope of boiling curves is very small for the single-phase region. There is a peak value for the curve, and after that, every configuration gradually decreased as the heat flux increased. For example, at heat flux of 30 W/cm2, the present study with 20μm micro-slots size has already reached the ONB condition. However, the plain wall microchannel and the previous structure remain in a single-phase region. As the number of micro-slots increases, the increasing nucleation sites lead to more effective nucleation boiling. Figure 3.5 (b) indicates the wall temperature of onset nucleation boiling as a heat flux function. Compared to the plain wall microchannels.

The present design shows a slight reduction of the wall temperature at the ONB owing to the increased number of nucleation sites. The overall wall superheats at T_{ONB} are approximately 13 ℃ different from the mass flux of 462 kg/m^{2}s, comparing the 10μm micro-slots structure to the plain wall microchannel configuration. Figure 3.5 (d) shows

that a peak CHF of 137W/cm^2 is obtained at a mass velocity of 1155 kg/m^{2}s, meaning a ~69% enhancement compared to the plain wall microchannel. As shown in Figure 3.5 (c), the two-phase pressure drop trend line on a full interconnected microchannel at a mass velocity of 924 kg/m^{2}s slightly decreases, which illustrates the pumping power budget was reduced. The gradually decreased pressure drop can be explained that the increased micro-slots' sizes can significantly release the two-phase pressure drop.

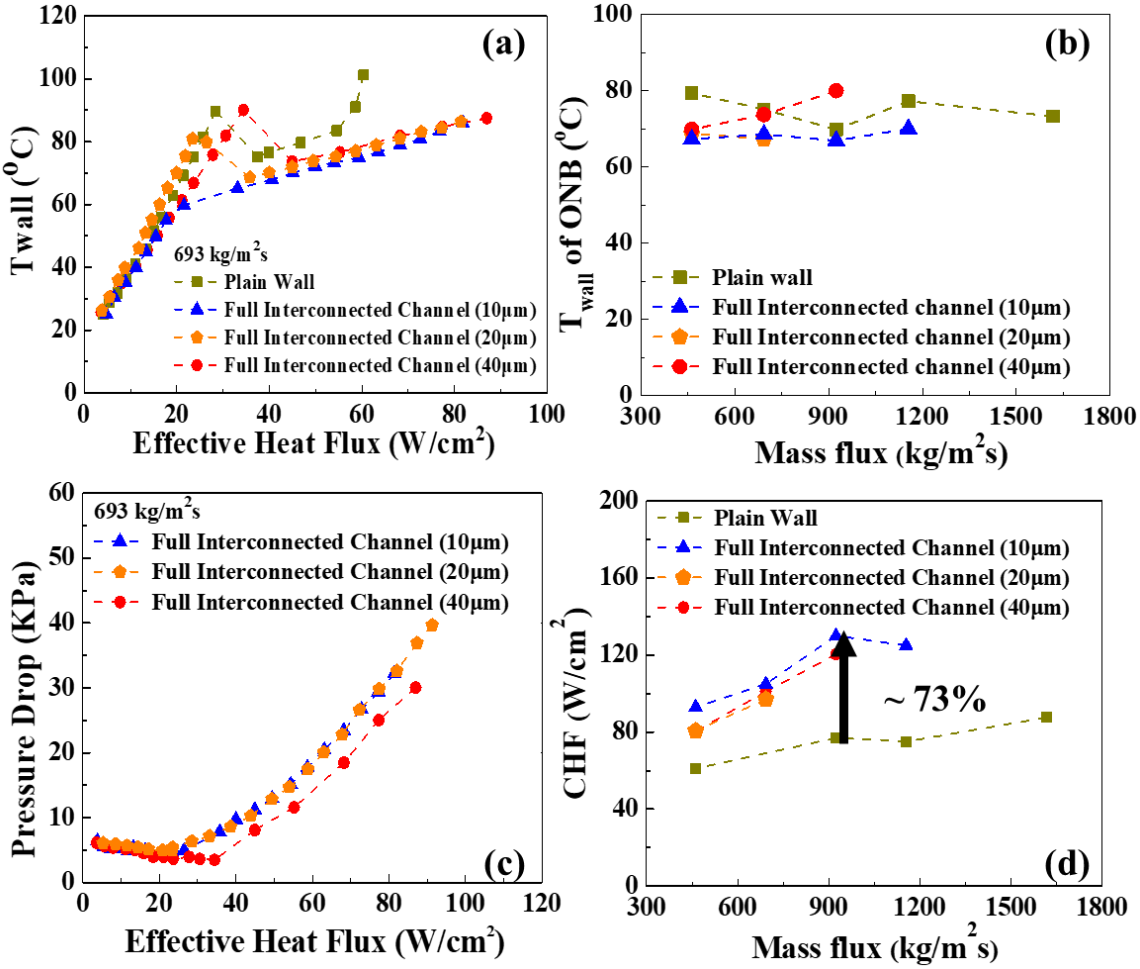

Figure 3.5 Comparisons of flow boiling performance on the present microchannel configuration and the previous studies of the half-interconnected channel and the plain wall microchannels. (a) Wall temperature as a function of effective heat flux at a mass flux of 693 kg/m^{2}s. (b) The onset of nucleation boiling of wall temperature as a function of mass flux. (c) Pressure drop as a function of effective heat flux. (d) CHF as a function of mass flux.

3.6 Bubble Dynamics

As previous study in half interconnected channels described, bubble departure frequency and bubble departure diameters are two important factors for flow boiling phenomenon and heat transfer performance mechanism study. Figure 3.6 (a) illustrates that bubble departure frequency using DI water as working fluid for fully interconnected microchannels has the same trend with the half interconnected microchannels with HFE-7100 as the working fluid. As the effective heat flux raises, the departure frequency increased. The maximum value of departure frequency was obtained at mass flux of 389 kg/m^{2}s of 4017 kHz. Improvement of the departure frequency can explain the high and rapid coordination of the rewetting phenomena inside the micro-slots, eventually delay local dryout, stabilize the nucleation boiling, enhance the HTC and extend the application range in engineering.

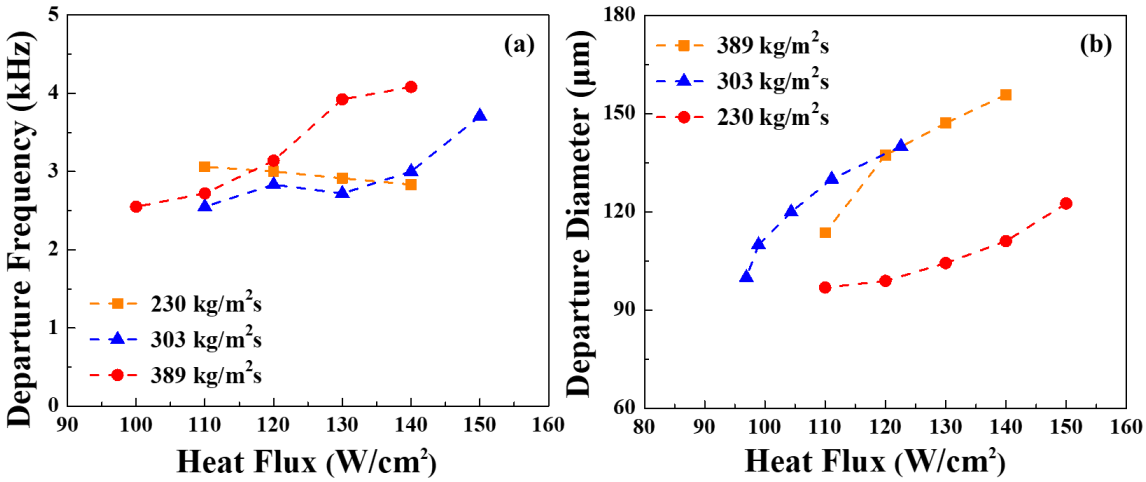

Figure 3.6 (a) Bubble departure frequency as a function of heat flux with DI water as the working fluid. (b) Bubble departure diameter as a function of heat flux.

Figure 3.6 (b) shows the bubble departure diameter as a function of heat flux. The bubble departure diameter slightly increased as the heat flux enhanced. A larger bubble diameter with higher departure frequency leads to better heat transfer performance due to

its capability to take away more heat from the fluid. As previous research described, in the interconnected microchannels with micro-slots, only a small amount of vapor could remain inside the micro-slots after the bubble departure because of the induced capillary pressure. Besides, the liquid can be quickly sucked into the slots during the bubble departure process and heated up after then, which keeps these micro-slots active all the time.

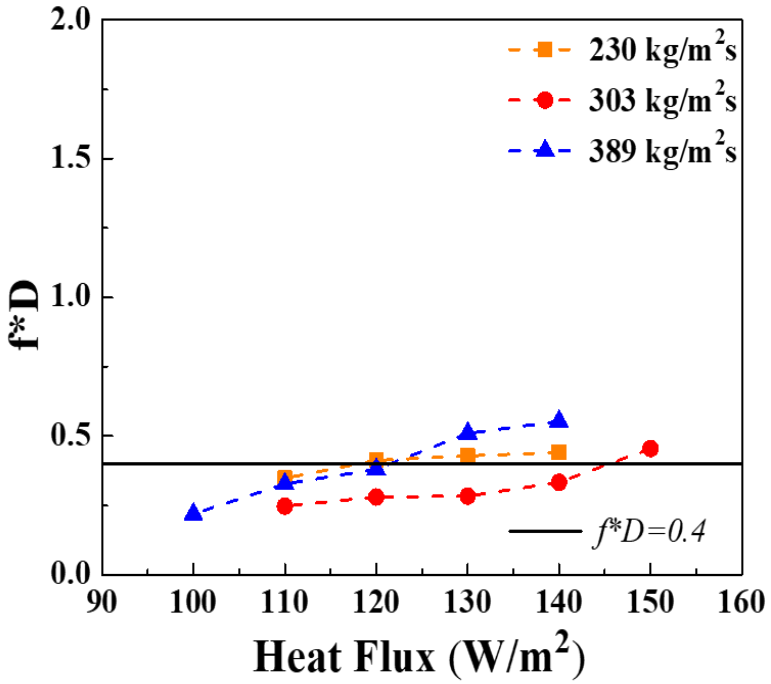

Figure 3.7 $f{\cdot}D$ as a function of heat flux with DI water as the working fluid.

Figure 3.7 proposed that the bubble departure diameter is closely related to the departure frequency with the fitting curve $f \cdot D_d = 0.4$, according to the previous report [130]. The curve-fitting experimental results are obtained from a visualization study captured by a high-speed camera.

3.7 Transient Study Analysis

Recent studies have revealed that flow boiling in micro-channels is associated with specific flow oscillations and instabilities related to the oscillation period [131]. The

previous study only focused on the steady state of the experiment, and some phenomena could not be captured before. Therefore, the transient study is developed to understand the underlying mechanism of flow boiling in microchannels deeply. In this study, full interconnected microchannels with 20μm micro-slot are used as test chips, HFE-7100 as working fluid.

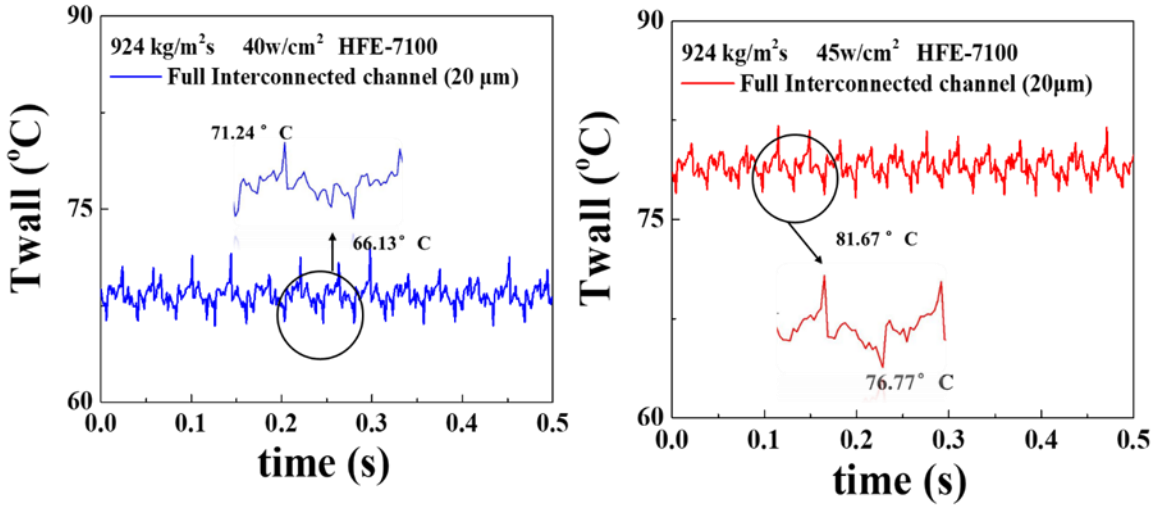

Figure 3.8 Comparison of the full interconnected channel with different heat flux at the mass flux of 924 kg/m^{2}s. Wall temperature as a function of time.

As shown in Figure 3.8 (a, b), at mass flux of 924 kg/m^{2}s, heat flux of 40 w/cm^2 and 45 w/cm^2, wall temperature oscillated along with the time. The maximum temperature difference between the channel wall is ~5 °C. As aforementioned, effective HTCs are significantly enhanced during the boiling nucleation region compared to the plain wall microchannel configuration. Figure 3.5 (b) indicates that compared to the plain wall microchannels, a significant reduction of T_{ONB} is observed in the enhanced nucleation boiling because of the increased number of nucleation sites. Figure 3.9 shows oscillation frequency in the plain wall microchannel is 5 Hz, much lower than the full interconnected channel with 33.75Hz. Like the previous study, the interconnected channel has a good

performance of sustaining nucleation boiling and delaying local dryout. The oscillation frequency can explain the reason of interconnected microchannel has more stability mechanism compared to plain wall microchannel. It is also clearly demonstrating that the trend line of wall temperature of plain wall microchannel is oscillated and has a large wave as shown in Figure 3.9, which can make clear reason for worse heat transfer performance in plain wall microchannels. The present design temperature fluctuates periodically and more stable compared to the chaotic fluctuation of plain wall microchannel. This indicates the introduction of micro-slots can effectively manage boiling instabilities.

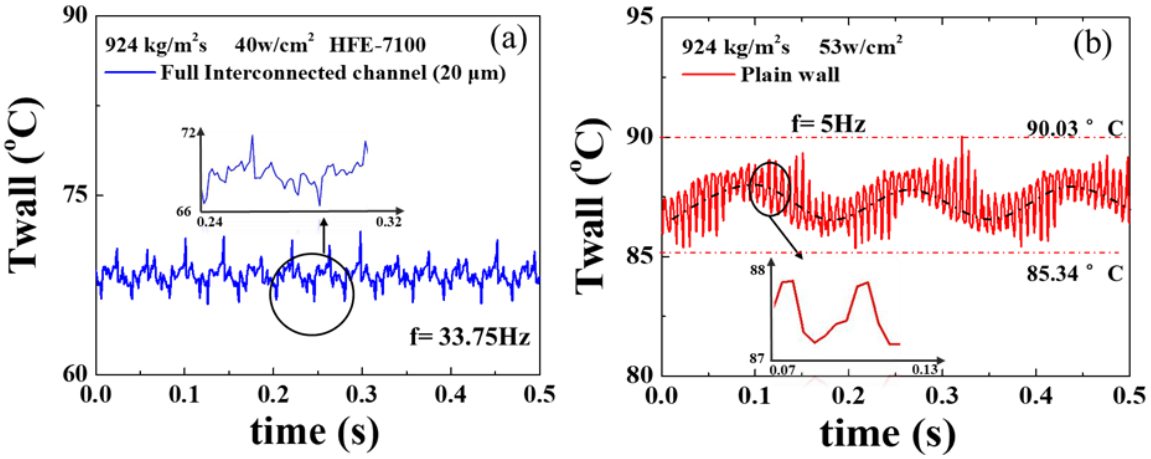

Figure 3.9 Comparing the full interconnected channel and plain wall microchannel with the same heat flux at the mass flux of 924 kg/m^{2}s. Wall temperature as a function of time.

3.8 Conclusions

In conclusion, the present microchannel configuration has been demonstrated to enhance flow boiling drastically. The continuous rewetting and sustainable global liquid supply have been substantially promoted by generating high-frequency jetting flows through the micro-slots. The main achievement, as shown below:

Compared to different sizes of micro-slots, the interconnected microchannel with 10μm micro-slots size has a significant enhancement of CHF with ~73% at mass flux of

924 kg/m^{2}s and CHF up to 134 W/cm^2. Pressure drops are reduced ~ 1.3 times compare to the 10μm micro-slots size to the 40μm micro-slots size. Wall temperature of ONB has been reduced, especially with interconnected microchannels of 10μm and 20μm. Effective HTC enhanced along with the micro-slot size decrease. The micro-slots size with 10μm has an almost 60% larger HTC than the micro slots size with 20um for present microchannels. The interconnected microchannel configuration is promising in implementing the two-phase cooling of high-power electronics. And the prediction of optimum working conditions with different micro-slots sizes has been obtained.

CHAPTER 4 THEORETICAL STUDIES OF BUBBLE DYNAMIC OF FLOW BOILING WITH DI WATER AND HEF-7100 IN FULL INTERCONNECTED MICROCHANNELS

To better understand the bubble dynamic mechanism, a theoretical study is conducted to understand and validate the working principle of microchannel structures bubble dynamic. As proposed in many studies [89, 102, 104, 130], to develop a theoretical bubble dynamic model for flow boiling in microchannels with high frequency rewetting and oscillations, all essential thermo-physical properties, for example, latent heat of evaporation, specific heat and heat conductivity need to be considered.

It is also challenging to develop a bubble dynamic model in a flow boiling considering the unstable flow conditions, irregulate bubble sizes, and the diversity of two-phase flow boiling. Thus, it is critical to take into account the different working fluid properties.

In this study, according to other bubble dynamic models and correlations in two-phase flow boiling heat transfer of microchannels, three nondimensional parameters related to bubble departure diameter, effective heat flux and bubble departure frequency were established. In this study, three approximate logarithmic relationships between the bubble departure diameter, bubble departure frequency, and the heat flux, bubble growth rate and time are obtained. The fitted bubble dynamic models agree well with existing data even if the data acquired from the different fluid mass flux, which confirmed the model is accurate.

4.1 Experimental Apparatus and Methods

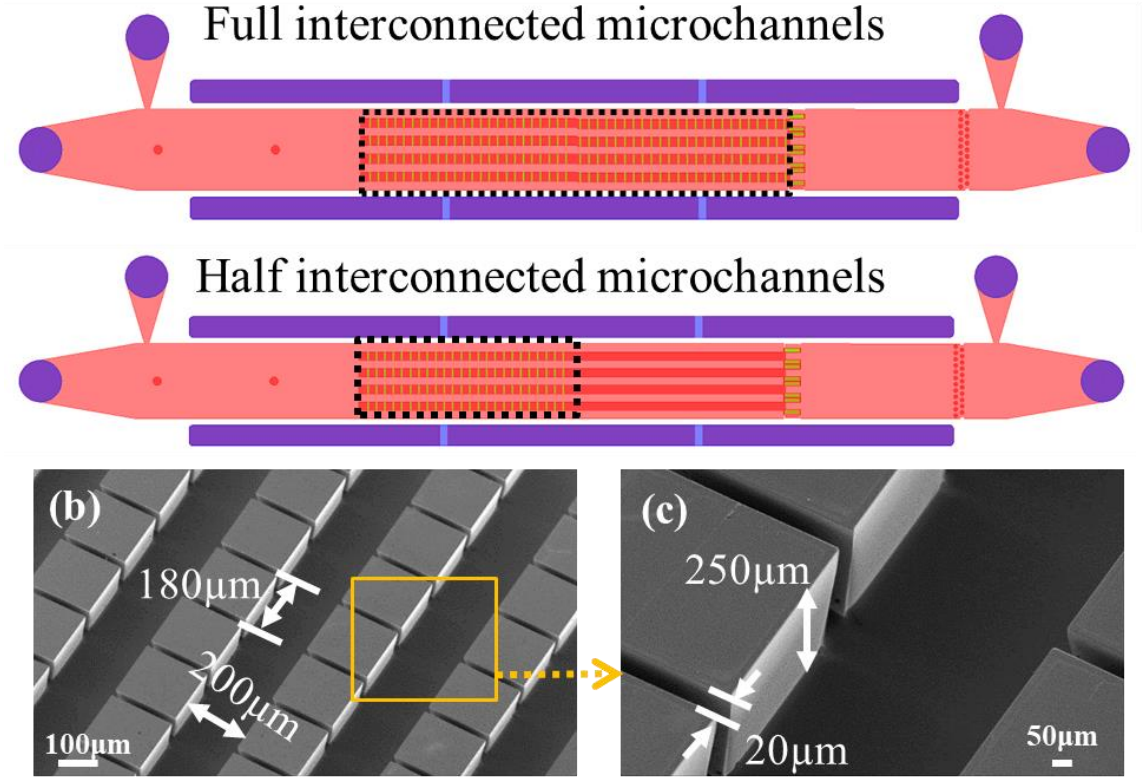

Figure 4.1 Schematic of the testing chip.

The approach developed in this study is the same as the one developed by Kuo [130] to analyze the bubble growth and departure during nucleate boiling on a horizontal surface. Microdevices with micro-slots as nucleation sites are designed to enhance and sustain the nucleation boiling in microchannels. Each device consists of 5 parallel microchannels (Length x Wide x Height = 10mm x 200μm x 250μm) are interconnected by 28 micro-slots (W=20μm) on each intermediate wall, as shown in Figure 4.1. The experiment apparatus details consist of the test loop, working principle, experiment procedure, data reduction, and bubble dynamic studies as established in previous studies.

The latest research indicated that the bubble dynamics of flow boiling include bubble departure diameter, bubble growth diameter, and bubble departure frequency

models. Therefore, bubble departure diameter, bubble growth diameter, and bubble departure frequency are collected from the earlier study in the last two chapters for varying mass flux and different working fluids such as DI water and HFE-7100.

4.2 Measurements

As proposed in the previous study [128], the test system was established to collect experimental data and capture movies with high-speed camera. The major components of the experimental setup of the open coolant loop are visualization system, data acquisition system, and microdevice package. A pressurized reservoir served as collection tank to supply working fluid for the experiments, such as HFE-7100 or DI water, which should be degassed first. High-pressure nitrogen is used as a pump. The working fluid pass through a mass flow meter of Krohne Optimass 3300c with ± 0.1% resolution (density with ± 2kh/m^3). The microdevice package details are presented in the previous study [128], two pressure transducers are for measuring the inlet and outlet absolute pressure difference. Two K-type thermocouples acquire the temperature from the inlet and outlet. The heater temperature is calculated by pre-calibrating the electric resistance of the microchip heater of the microchip as a linear function of working temperature. The electrical power is supplied by a high precision digital programmable power supply (BK-PRECISION XLN10014). The experimental data, such as flow rate, local pressure, inlet, and outlet temperature, voltage, resistance, and current, are collected by an Agilent 34972A data acquisition system and recorded by a customized data acquisition system with NI LabVIEW. A high-speed camera (Phantom V 7.3) and an Olympus microscope (BX-51) with 400× amplifications are used for the visualization study. All measurements are carried out at 1 atm ambient pressure and room temperature of 18 °C.

4.3 Data Comparison

The growing characteristics of vapor bubbles in the thermal boundary layer region near the superheated surface are more complex than the normal circumstances because of the lack of spherical symmetry and non-uniformity of temperature field of the surrounding liquid. Despite these significant differences, bubble growth near superheated surface exhibits an inertia-controlled regime and heat transfer controlled growth similar to those for spherical bubble growth in an infinite uniformly superheated ambient.

The bubble growth process near a heated wall can be idealized as a sequence of stages indicated schematically in Figure 4.2. After the departure of a bubble, liquid at the bulk fluid temperature T_∞ is brought into contact with the adjacent fluid with surface temperature $T_w > T_{sat}(P_\infty)$. A short period of time then elapses during which transient heat conduction into liquid takes place, but the bubbles likely do not grow up significantly. This time interval is referred to the waiting period, designated here as t_w.

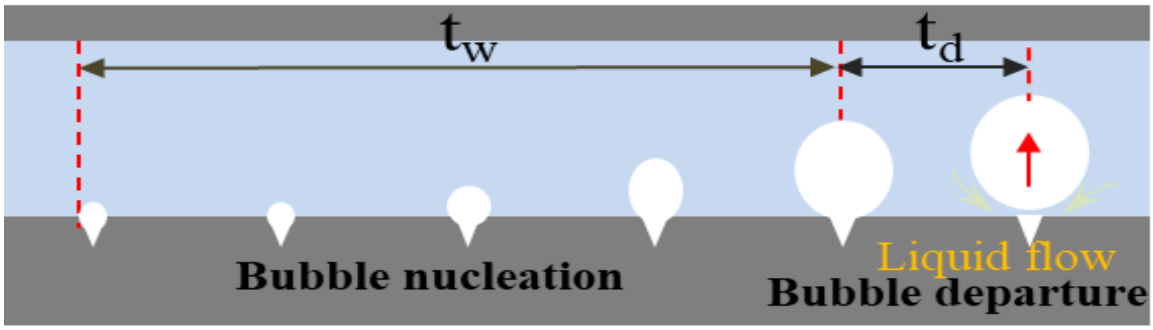

Figure 4.2 The waiting period and subsequent growth and release of a vapor bubble at an active cavity site.

Once the bubble growth begins, the thermal energy needed to vaporize liquid at the interface comes, at least in part, from the liquid region adjacent to the superheated bubble during the waiting period. During the initial stage of bubble growth, the liquid immediately

adjacent to the interface is highly superheated, and the heat transfer to the interface is not a limiting factor. As the embryo bubble emerges from the nucleation site cavity, a rapid expansion is triggered by the sudden increase in the radius of the curvature of bubble. The resulting rapid growth of the bubble is resisted primarily by the inertia of the liquid [132]. For this inertia controlled the early stage of the bubble growth process, the bubble grows nearly hemispherical. As the bubble grows up radially in this regime, a thin microlayer of liquid is left between the lower portion of the bubble interface and the heated wall. This liquid film, which is sometimes referred to as the evaporation microlayer, varies at the edge of the hemispherical bubble. Heat is transferred across this film from the wall to the interface, directly vaporizing liquid. This film may evaporate completely near the cavity where nucleation began, significantly elevating the surface temperature there. When this occurs, the surface temperature may fluctuate strongly during the repeated growth and release of bubbles as the surface cyclically dries out and then rewets.

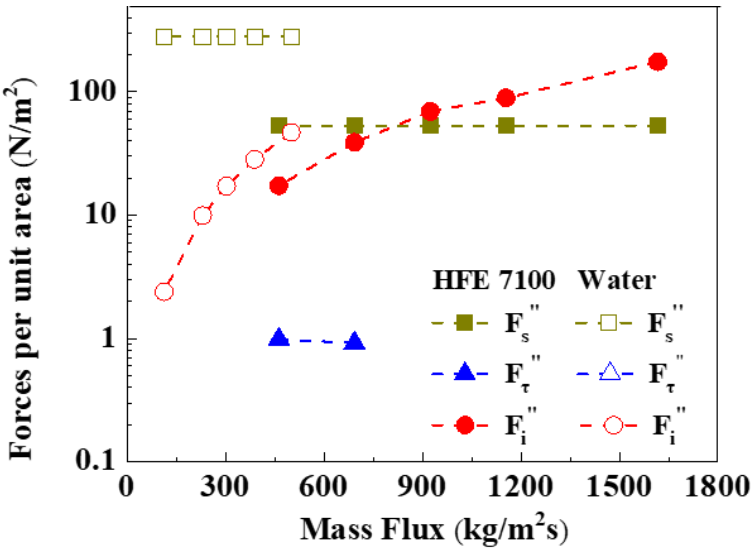

Figure 4.3 Forces per unit as a function of mass flux.

It is critical to learn from visualization results of bubble dynamics of flow boiling. Consequently, a high-fidelity prediction model could be developed. In this study,

comparison of the experimental data and different prediction models of bubble departure frequency and bubble departure diameter reported in the last decade is plotted (Figure 1.2). As shown in Figure 1.2 (a), the present experimental data has a higher departure frequency. The maximum frequency has achieved a value of ~7700 kHz at heat flux of 33 W/cm^2. Figure 1.2 (b) shows that the present experimental data of bubble departure diameter is much higher than the prediction of the developed models. However, it is still hard to illustrate the precise trend due to the significant variations in microchannels for the present experimental conditions, channel dimensions and working fluid. Therefore, the nondimensional model is needed and important.

Various forces acting on the liquid-vapor interface, including inertia force, surface tension, shear stress, buoyancy, and evaporation momentum, significantly affect the two-phase flow and heat transfer. The previous studies [67, 76] have analyzed the forces acting on the liquid-vapor interface. In this study, simplified equations are adopted from the study [76] to calculate these forces.

Surface tension per unit area,

$$F_s^{"} = \frac{\sigma \cdot \cos \vartheta \cdot D}{A_c} \tag{26}$$

Where A_c is the channel cross-section area.

Inertia force per unit area,

$$F_i^{"} = \rho \cdot U^2 \tag{27}$$

The shear stress is expressed as,

$$F_\tau^{"} = \frac{\mu \cdot U \cdot A_{pl}}{D \cdot A_c} \tag{28}$$

Buoyancy force per unit area,

$$F_b^{"} = (\rho_v - \rho_l) \cdot g \cdot \cos\varphi \cdot \frac{V}{A_c} \tag{29}$$

Figure 4.3 indicates the comparison of shear stress, inertia force, and the surface tension for water and HFE-7100 at different mass fluxes. The surface tension force and inertia force of HFE-7100 are lower than those of water. However, the sheer stress of HFE-71000 is higher than that of water due to its large dynamic viscosity. From Figure 4.3, it also can be found that the inertia and shear forces increase with the mass flux increasing. Surface tension is dominant at relatively low mass fluxes but suppressed by inertia force with increased mass flux. The higher surface tension force and inertia force can facilitate thin liquid film formation and enhance rewetting. Hence, the flow boiling performances on water outperform that on HFE-7100.

4.4 Results and Discussion

If the bubble growth process does become heat transfer controlled, pressure and liquid inertia force become relatively smaller, and surface tension then tends to pull the bubble to a more spherical shape. Thus, it undergoes the transition from inertia controlled growth to heat transfer controlled growth, the shape of the bubble is transformed from a hemispherical shape to a more spherical configuration, as indicated in Figure 4.2.

Throughout the bubble growth process, interfacial tension acting along the contact line tends to hold the bubble in place on the surface. Buoyancy, shear stress, buoyancy, and inertia forces associated with the motion of the surrounding fluid may act to pull the bubble away. These detaching forces generally become stronger as the bubble becomes larger. As shown in Figure 4.3, when the net force effect becomes large enough, the retaining effect of surface tension forces at the contact line is overcome, the bubble would release accordingly.

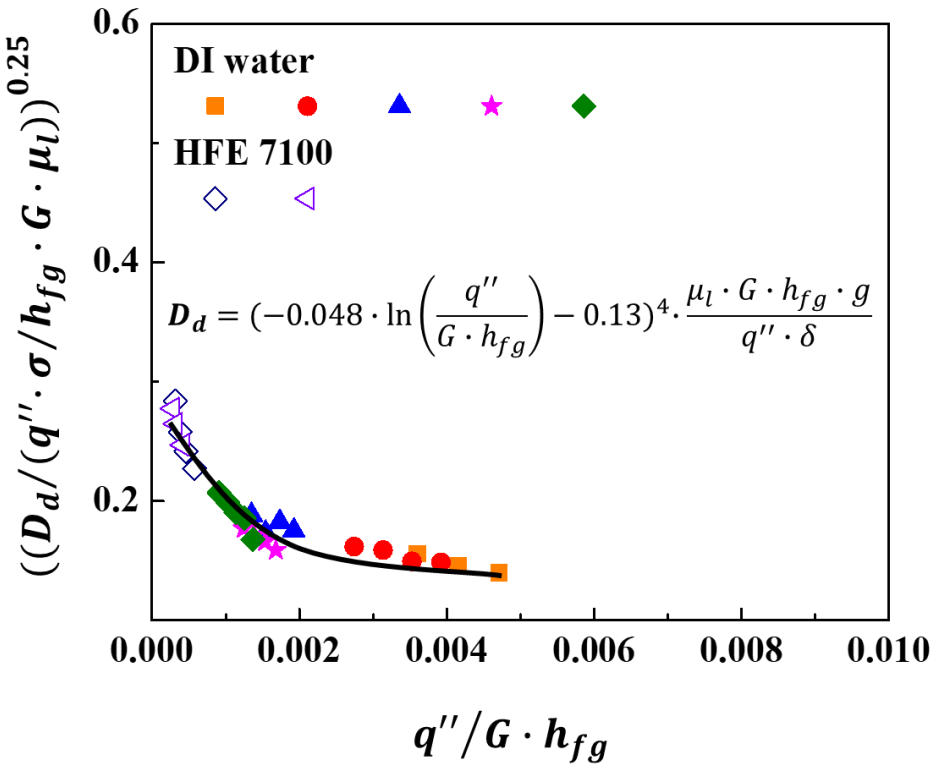

Figure 4.4 Non-dimensional study of bubble departure diameter.

As the above analysis admits the possibility of both inertia controlled and heat transfer controlled growth regimes, the occurrence or absence of either one depends on the conditions under which bubble growth occurs. Specifically, very rapid, inertia controlled growth is more likely to take place as the following conditions exist: high wall superheat, high imposed heat flux, highly polished surface having only very small cavities, very low contact angle (highly wetting liquid), low latent heat of vaporization, low system pressure (resulting in low vapor density).

The bubble departure frequency, bubble growth diameter, and bubble departure diameter are rarely seen in flow boiling area in the last decade. It is extremely challenging to modify a theoretical model that coincides with the experimental data. According to the present experimental situations, assuming bubble departure diameter, bubble departure

frequency, and bubble growth diameter is related to the density, latent heat of vaporization, surface tension, the thermal conductivity of working fluids, mass flux, and gravity of the earth, and heat flux.

$$D_d = (-0.048 \cdot \ln(\frac{q^{"}}{G \bullet h_{fg}}) - 0.13)^{0.25} \cdot \mu_l \cdot G \cdot h_{fg} \cdot g / q^{"} \cdot \delta \tag{30}$$

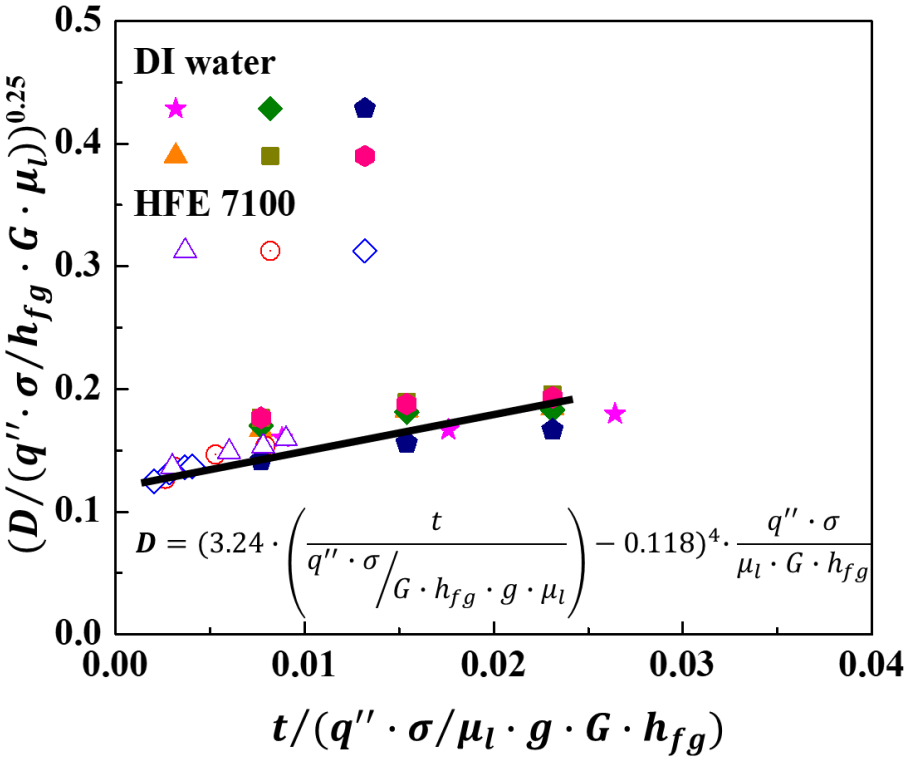

Figure 4.5 Non-dimensional study of bubble growth diameter.

Figure 4.4 demonstrates an approximate logarithmic relationship between the bubble departure diameter and the heat flux that the equation shows in Eq 30. As shown in Figure 4.4, an approximate logarithmic relationship between the bubble departure diameter and the heat flux is obtained. The fitted bubble dynamic model agrees well with the present experimental data for water and HFE-7100 as the working fluids, which confirmed the model accurately.

The bubble departure diameter served as y-coordinate nondimensionalized with heat flux, liquid thermal conductivity, latent heat, mass flux, and surface tension. An exponent correlation is applied to obtain a more consistent curve.

$$D = (3.24 \cdot \frac{t / q^{"} \cdot \delta}{\mu_l \cdot G \cdot h_{fg} \cdot g}) - 0.118)^{0.25} \cdot q^{"} \cdot \delta / \mu_l \cdot G \cdot h_{fg} \tag{31}$$

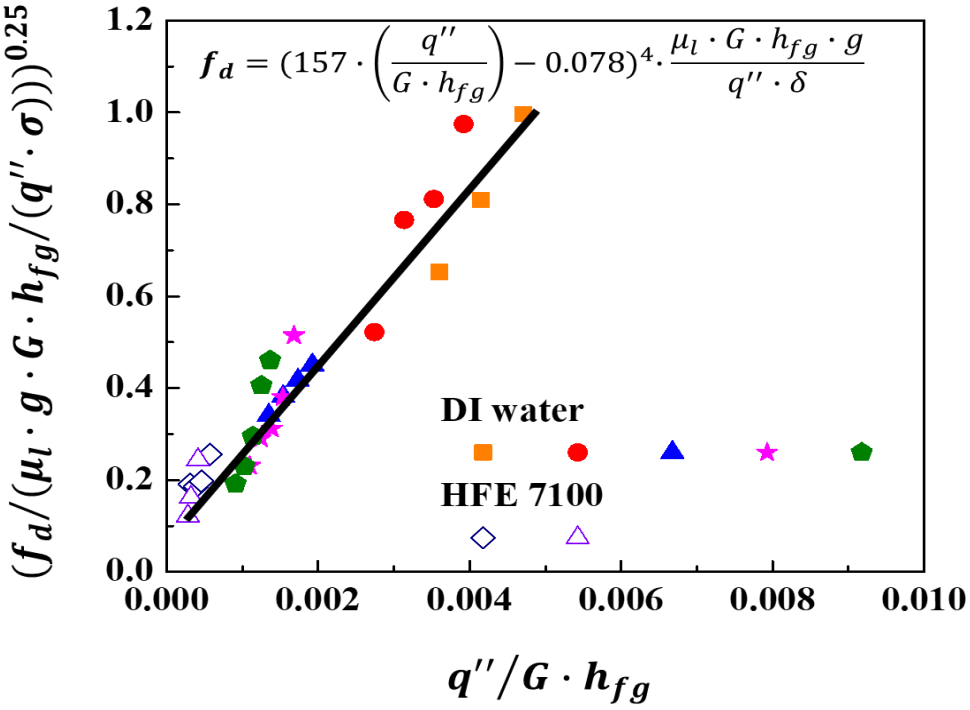

Figure 4.6 Non-dimensional study of bubble departure frequency.

Figure 4.5 illustrates the relationship between the bubble growth diameter and time. There is an approximately linear relationship between the growth diameter and the time. Similarly, two parameters are established, which are related to bubble growth diameter and time, respectively. The fitted bubble dynamic model agrees well with existing experimental data. Eq 31 is the data trend line in Figure 4.5. Based on Figure 2.7(b), the prediction models are fitted very well with the experimental data for nine different working conditions.

$$f_d = (157 \cdot \frac{q^{"}}{G \bullet h_{fg}} - 0.078)^{0.25} \cdot \mu_l \cdot G \cdot h_{fg} \cdot g / q^{"} \cdot \delta \quad (32)$$

Figure 4.6 shows the linear relationship between the bubble departure frequency and heat flux. The maximum relative deviation is about 19%. As shown in Figure 2.12 (a), the experimental data collected by high-speed camera, the seven different flow conditions with two different working fluids, has basically fallen into a linear trend line, which shows the prediction model for the bubble departure frequency is feasible . The linear relationship equation has shown as Eq 32.

4.5 Conclusions

In this study, a nondimensional study of bubble dynamics in microchannels with bubble departure diameter, bubble growth diameter, and bubble departure frequency are experimentally and theoretically studied. The semi theoretical bubble dynamic models are developed based on the latent heat, surface tension, and liquid viscosity of the different working fluids. Previous bubble departure diameter, growth diameter, and bubble departure frequency models and correlations are compared to the present theoretical model. Major conclusions are summarized as follow:

The theoretical bubble dynamics models developed in this study considers the effects of thermophysical properties, geometries, and flow conditions. The development of the theoretical bubble dynamics model provides insights into the dynamic bubble mechanisms. However, further investigation is needed to estimate accurate local subcooling and interfacial vapor to liquid heat transfer coefficient. Existing recognized bubble dynamics correlations in microchannels are also compared to the present study. The semi-empirical correlation developed by Cuo shows a great agreement with the

experimental data because of the similarities in the microchannel configuration and heat transfer mechanisms.

REFERENCES

1. Prajapati, Y.K. and P. Bhandari, *Flow boiling instabilities in microchannels and their promising solutions–A review.* Experimental Thermal and Fluid Science, 2017. **88**: p. 576-593.

2. Huh, C., J. Kim, and M.H. Kim, *Flow pattern transition instability during flow boiling in a single microchannel.* International Journal of Heat and Mass Transfer, 2007. **50**(5-6): p. 1049-1060.

3. Qu, W. and I. Mudawar, *Flow boiling heat transfer in two-phase micro-channel heat sinks—II. Annular two-phase flow model.* International Journal of Heat and Mass Transfer, 2003. **46**(15): p. 2773-2784.

4. Ory, E., et al., *Growth and collapse of a vapor bubble in a narrow tube.* Physics of fluids, 2000. **12**(6): p. 1268-1277.

5. Kobayashi, J., et al., *A microfluidic device for conducting gas-liquid-solid hydrogenation reactions.* Science, 2004. **304**(5675): p. 1305-1308.

6. Kandlikar, S.G., *History, advances, and challenges in liquid flow and flow boiling heat transfer in microchannels: a critical review.* Journal of heat transfer, 2012. **134**(3).

7. Schneider, B., et al., *Cavitation enhanced heat transfer in microchannels.* 2006.

8. Li, C., et al., *Nanostructured copper interfaces for enhanced boiling.* small, 2008. **4**(8): p. 1084-1088.

9. Kandlikar, S.G., *Fundamental issues related to flow boiling in minichannels and microchannels.* Experimental Thermal and Fluid Science, 2002. **26**(2-4): p. 389-407.

10. Agostini, B., et al., *High heat flux two-phase cooling in silicon multimicrochannels.* IEEE Transactions on Components and Packaging Technologies, 2008. **31**(3): p. 691-701.

11. Zhu, Y., et al., *Surface structure enhanced microchannel flow boiling.* Journal of Heat Transfer, 2016. **138**(9).

12. Bouré, J., A. Bergles, and L. Tong, *Review of Two-Phase Flow Instability, Nuclear Engineering and Design 25*. 1973, North-Holland Publishing Company.

13. Moreno Quiben, J., *Experimental and analytical study of two-phase pressure drops during evaporation in horizontal tubes*. 2005, EPFL.

14. Ledinegg, M., *Instability flow during natural forced circulation.* Warme, 1938. **61**: p. 891-898.

15. Kakac, S. and T. Veziroglu, *A review of two-phase flow instabilities,* in *Advances in Two-phase Flow and Heat Transfer*. 1983, Springer. p. 577-667.

16. Wallis, G. and J. Heasley, *Oscillations in two-phase flow systems.* Journal of Heat Transfer, 1961. **83**(3).

17. Quandt, E. *Analysis and measurement of flow oscillations*. in *Chemical Engineering Progress Symposium Series*. 1961.

18. Kuang, Y., et al., *Flow boiling of ammonia and flow instabilities in mini-channels.* Applied Thermal Engineering, 2017. **113**: p. 831-842.

19. Alugoju, U.K., S.K. Dubey, and A. Javed, *3D Transient heat transfer analysis and flow visualization study in diverging microchannel for instability mitigated two-phase flow: A numerical study.* International Journal of Heat and Mass Transfer, 2020. **160**: p. 120212.

20. Xu, F., H. Wu, and Z. Liu, *Flow patterns during flow boiling instability in silicon-based pin-fin microchannels.* Journal of Heat Transfer, 2018. **140**(3).

21. Özdemir, M.R., *A review of single-phase and two-phase pressure drop characteristics and flow boiling instabilities in microchannels.* Journal of Thermal Engineering, 2018. **4**(6): p. 2451-2463.

22. Huang, H., L.-m. Pan, and R.-g. Yan, *Flow characteristics and instability analysis of pressure drop in parallel multiple microchannels.* Applied Thermal Engineering, 2018. **142**: p. 184-193.

23. Chen, X., et al., *An experimental investigation of flow boiling instability in a natural circulation loop.* International Journal of Heat and Mass Transfer, 2018. **117**: p. 1125-1134.

24. Chen, S., et al., *Flow boiling instability of liquid nitrogen in horizontal mini channels.* Applied Thermal Engineering, 2018. **144**: p. 812-824.

25. Cui, F., et al., *Two-phase flow instability in distributed jet array impingement boiling on pin-fin structured surface and its affecting factors.* International Journal of Heat and Mass Transfer, 2019. **143**: p. 118495.

26. Morshed, A., et al., *Enhanced flow boiling in a microchannel with integration of nanowires.* Applied Thermal Engineering, 2012. **32**: p. 68-75.

27. Sitar, A. and I. Golobic, *Heat transfer enhancement of self-rewetting aqueous n-butanol solutions boiling in microchannels.* International Journal of Heat and Mass Transfer, 2015. **81**: p. 198-206.

28. Carey, V.P., *Liquid-vapor phase-change phenomena: an introduction to the thermophysics of vaporization and condensation processes in heat transfer equipment*. 2020: CRC Press.

29. Huang, G., et al., *High-frequency alternating nucleate boiling of water enabled by microslot arrays in microchannels.* International Journal of Heat and Mass Transfer, 2020. **150**: p. 119271.

30. Zhang, T., et al., *Stability analysis and maldistribution control of two-phase flow in parallel evaporating channels.* International Journal of Heat and Mass Transfer, 2011. **54**(25-26): p. 5298-5305.

31. Park, I.W., et al., *Can flow oscillations during flow boiling deteriorate the heat transfer coefficient?* Applied Physics Letters, 2018. **113**(15): p. 154102.

32. Zhu, H., et al., *Investigation of fatigue behavior of Pb (Zr0. 45Ti0. 55) O3 thin films under asymmetric polarization switching.* Japanese Journal of Applied Physics, 2016. **55**(9): p. 091501.

33. Kharangate, C.R., L.E. O'Neill, and I. Mudawar, *Effects of two-phase inlet quality, mass velocity, flow orientation, and heating perimeter on flow boiling in a rectangular channel: Part 1–Two-phase flow and heat transfer results.* International journal of heat and mass transfer, 2016. **103**: p. 1261-1279.

34. Lu, C.T. and C. Pan, *A highly stable microchannel heat sink for convective boiling.* Journal of Micromechanics and microengineering, 2009. **19**(5): p. 055013.

35. Chang, J. and S. You, *Boiling heat transfer phenomena from microporous and porous surfaces in saturated FC-72.* International Journal of Heat and Mass Transfer, 1997. **40**(18): p. 4437-4447.

36. El-Genk, M.S. and J.L. Parker, *Enhanced boiling of HFE-7100 dielectric liquid on porous graphite.* Energy Conversion and Management, 2005. **46**(15-16): p. 2455-2481.

37. Yang, K.-S., et al., *Heat transfer and flow pattern characteristics for HFE-7100 within microchannel heat sinks.* Heat transfer engineering, 2011. **32**(7-8): p. 697-704.

38. Yang, F., et al., *Flow boiling phenomena in a single annular flow regime in microchannels (I): Characterization of flow boiling heat transfer.* International Journal of Heat and Mass Transfer, 2014. **68**: p. 703-715.

39. Kuo, C.-J. and Y. Peles, *Flow boiling instabilities in microchannels and means for mitigation by reentrant cavities.* Journal of Heat Transfer, 2008. **130**(7).

40. Lee, D.-Y. and K. Vafai, *Analytical characterization and conceptual assessment of solid and fluid temperature differentials in porous media.* International Journal of Heat and Mass Transfer, 1999. **42**(3): p. 423-435.

41. Hasan, M.I., *Investigation of flow and heat transfer characteristics in micro pin fin heat sink with nanofluid.* Applied thermal engineering, 2014. **63**(2): p. 598-607.

42. Koşar, A., C.-J. Kuo, and Y. Peles, *Suppression of boiling flow oscillations in parallel microchannels by inlet restrictors.* Journal of Heat Transfer, 2006. **128**(3): p. 251-260.

43. Kuo, C.-J. and Y. Peles, *Local measurement of flow boiling in structured surface microchannels.* International journal of heat and mass transfer, 2007. **50**(23-24): p. 4513-4526.

44. Wang, E.N., et al., *Micromachined jets for liquid impingement cooling of VLSI chips.* Journal of Microelectromechanical systems, 2004. **13**(5): p. 833-842.

45. Stroock, A.D., et al., *Chaotic mixer for microchannels.* Science, 2002. **295**(5555): p. 647-651.

46. Li, W., J. Ma, and C. Li, *Enhanced flow boiling in microchannels by incorporating multiple micro-nozzles and micro-pinfin fences.* International Journal of Heat and Mass Transfer, 2020: p. 120695.

47. Wang, G., P. Cheng, and A. Bergles, *Effects of inlet/outlet configurations on flow boiling instability in parallel microchannels.* International Journal of Heat and Mass Transfer, 2008. **51**(9-10): p. 2267-2281.

48. Kalani, A. and S. Kandlikar, *Combining liquid inertia with pressure recovery from bubble expansion for enhanced flow boiling.* Applied Physics Letters, 2015. **107**(18): p. 181601.

49. Singh, N., et al., *Flow boiling enhancement on a horizontal heater using carbon nanotube coatings.* International Journal of Heat and Fluid Flow, 2010. **31**(2): p. 201-207.

50. Sarwar, M.S., Y.H. Jeong, and S.H. Chang, *Subcooled flow boiling CHF enhancement with porous surface coatings.* International journal of heat and mass transfer, 2007. **50**(17-18): p. 3649-3657.

51. You, S., J. Kim, and K. Kim, *Effect of nanoparticles on critical heat flux of water in pool boiling heat transfer.* Applied physics letters, 2003. **83**(16): p. 3374-3376.

52. O'Hanley, H., et al., *Separate effects of surface roughness, wettability, and porosity on the boiling critical heat flux.* Applied Physics Letters, 2013. **103**(2): p. 024102.

53. Kim, B.S., et al., *Interfacial wicking dynamics and its impact on critical heat flux of boiling heat transfer.* Applied Physics Letters, 2014. **105**(19): p. 191601.

54. Kim, D.E., et al., *Enhanced critical heat flux by capillary driven liquid flow on the well-designed surface.* Applied Physics Letters, 2015. **107**(2): p. 023903.

55. Chu, K.-H., R. Enright, and E.N. Wang, *Structured surfaces for enhanced pool boiling heat transfer.* Applied Physics Letters, 2012. **100**(24): p. 241603.

56. Wang, Q. and R. Chen, *Ultrahigh flux thin film boiling heat transfer through nanoporous membranes.* Nano letters, 2018. **18**(5): p. 3096-3103.

57. Li, W., et al., *Enhanced flow boiling in microchannels through integrating multiple micro-nozzles and reentry microcavities.* Applied Physics Letters, 2017. **110**(1): p. 014104.

58. Koşar, A., C.-J. Kuo, and Y. Peles, *Suppression of boiling flow oscillations in parallel microchannels by inlet restrictors.* 2006.

59. Kandlikar, S.G., et al., *Stabilization of flow boiling in microchannels using pressure drop elements and fabricated nucleation sites.* 2006.

60. Koşar, A., C.-J. Kuo, and Y. Peles, *Boiling heat transfer in rectangular microchannels with reentrant cavities.* International Journal of Heat and Mass Transfer, 2005. **48**(23-24): p. 4867-4886.

61. Xia, G., et al., *Optimum thermal design of microchannel heat sink with triangular reentrant cavities.* Applied Thermal Engineering, 2011. **31**(6-7): p. 1208-1219.

62. Krishnamurthy, S. and Y. Peles, *Flow boiling of water in a circular staggered micro-pin fin heat sink.* International Journal of Heat and Mass Transfer, 2008. **51**(5-6): p. 1349-1364.

63. Stroock, A.D., et al., *Patterning flows using grooved surfaces.* Analytical chemistry, 2002. **74**(20): p. 5306-5312.

64. Chen, T. and S.V. Garimella, *Measurements and high-speed visualizations of flow boiling of a dielectric fluid in a silicon microchannel heat sink.* International Journal of Multiphase Flow, 2006. **32**(8): p. 957-971.

65. Yang, F., et al., *Flow boiling heat transfer of HFE-7000 in nanowire-coated microchannels.* Applied Thermal Engineering, 2016. **93**: p. 260-268.

66. Kuo, C.J. and Y. Peles, *Flow Boiling of Coolant (HFE-7000) Inside Structured and Plain Wall Microchannels.* Journal of Heat Transfer, 2009. **131**(12): p. 121011.

67. Li, W., et al., *Flow boiling of HFE-7100 in silicon microchannels integrated with multiple micro-nozzles and reentry micro-cavities.* International Journal of Heat and Mass Transfer, 2018. **123**: p. 354-366.

68. Parker, J.L. and M.S. El-Genk, *Enhanced saturation and subcooled boiling of FC-72 dielectric liquid.* International Journal of Heat and Mass Transfer, 2005. **48**(18): p. 3736-3752.

69. Chang, J.Y. and S.M. You, *Boiling heat transfer phenomena from microporous and porous surfaces in saturated FC-72.* International Journal of Heat and Mass Transfer, 1997. **40**: p. 4437-4447.

70. Wang, C.-C., et al., *Effect of inclination on the convective boiling performance of a microchannel heat sink using HFE-7100.* Experimental Thermal and Fluid Science, 2012. **36**: p. 143-148.

71. Hetsroni, G., et al., *Explosive boiling of water in parallel micro-channels.* International Journal of Multiphase Flow, 2005. **31**(4): p. 371-392.

72. Yusheng Dou, L.V.Z., Nicholas Winograd, and Barbara J. Garrison, *Explosive Boiling of Water Films Adjacent to Heated Surfaces-A Microscopic Description.* Journal of Physics Chemistry A, 2001. **105**: p. 2748-2755.

73. Koşar, A., C.-J. Kuo, and Y. Peles, *Suppression of Boiling Flow Oscillations in Parallel Microchannels by Inlet Restrictors.* Journal of Heat Transfer, 2006. **128**(3): p. 251-260.

74. Kuo, C.J. and Y. Peles, *Local measurement of flow boiling in structured surface microchannels.* International Journal of Heat and Mass Transfer, 2007. **50**(23-24): p. 4513-4526.

75. Lee, J. and I. Mudawar, *Fluid flow and heat transfer characteristics of low temperature two-phase micro-channel heat sinks – Part 1: Experimental methods and flow visualization results.* International Journal of Heat and Mass Transfer, 2008. **51**(17-18): p. 4315-4326.

76. Alam, T., et al., *Force analysis and bubble dynamics during flow boiling in silicon nanowire microchannels.* International Journal of Heat and Mass Transfer, 2016. **101**: p. 915-926.

77. Costa-Patry, E. and J.R. Thome, *Flow pattern-based flow boiling heat transfer model for microchannels.* International Journal of Refrigeration, 2013. **36**(2): p. 414-420.

78. Wojtan, L., T. Ursenbacher, and J.R. Thome, *Investigation of flow boiling in horizontal tubes: Part I—A new diabatic two-phase flow pattern map.* International journal of heat and mass transfer, 2005. **48**(14): p. 2955-2969.

79. Kattan, N., J.R. Thome, and D. Favrat, *Flow boiling in horizontal tubes: part 3—development of a new heat transfer model based on flow pattern.* 1998.

80. Dong, Z., et al., *Numerical study of vapor bubble effect on flow and heat transfer in microchannel.* International journal of thermal sciences, 2012. **54**: p. 22-32.

81. Mukherjee, A. and S. Kandlikar, *The effect of inlet constriction on bubble growth during flow boiling in microchannels.* International Journal of Heat and Mass Transfer, 2009. **52**(21-22): p. 5204-5212.

82. Hibiki, T. and M. Ishii, *Active nucleation site density in boiling systems.* International Journal of Heat and Mass Transfer, 2003. **46**(14): p. 2587-2601.

83. Basu, N., G.R. Warrier, and V.K. Dhir, *Onset of nucleate boiling and active nucleation site density during subcooled flow boiling.* J. Heat Transfer, 2002. **124**(4): p. 717-728.

84. Hsu, Y., *On the size range of active nucleation cavities on a heating surface.* 1962.

85. Dhir, V.K., H.S. Abarajith, and D. Li, *Bubble dynamics and heat transfer during pool and flow boiling.* Heat Transfer Engineering, 2007. **28**(7): p. 608-624.

86. Benjamin, R. and A. Balakrishnan, *Nucleation site density in pool boiling of saturated pure liquids: effect of surface microroughness and surface and liquid physical properties.* Experimental Thermal and Fluid Science, 1997. **15**(1): p. 32-42.

87. Gunther, F.C., *Photographic study of surface-boiling heat transfer to water forced convection.* Trans. ASME, 1951. **73**: p. 115-123.

88. Friz, W., *Maximum volume of vapor bubbles.* Physic. Zeitschz., 1935. **36**: p. 379-354.

89. Klausner, J., et al., *Vapor bubble departure in forced convection boiling.* International journal of heat and mass transfer, 1993. **36**(3): p. 651-662.

90. Cole, R. and W. Rohsenow. *Correlation of bubble departure diameters for boiling of saturated liquids*. in *Chem. Eng. Prog. Symp. Ser*. 1969. 211 213.

91. Zeng, L., et al., *A unified model for the prediction of bubble detachment diameters in boiling systems—II. Flow boiling.* International journal of heat and mass transfer, 1993. **36**(9): p. 2271-2279.

92. Thorncroft, G., J. Klausnera, and R. Mei, *An experimental investigation of bubble growth and detachment in vertical upflow and downflow boiling.* International Journal of Heat and Mass Transfer, 1998. **41**(23): p. 3857-3871.

93. Situ, R., et al., *Bubble lift-off size in forced convective subcooled boiling flow.* International Journal of Heat and Mass Transfer, 2005. **48**(25-26): p. 5536-5548.

94. Fritz, W., *Berechnung des maximalvolumes von dampfblasen.* Physik. Zeitschr, 1935. **36**: p. 379-384.

95. Zuber, N. and J. Findlay, *Average volumetric concentration in two-phase flow systems.* 1965.

96. Ruckenstein, E., *A physical model for nucleate boiling heat transfer.* International Journal of Heat and Mass Transfer, 1964. **7**(2): p. 191-198.

97. Mikic, B., *Bubble growth rates in non-uniform temperature field.* Progress in Heat and Mass Transfer, 1969. **2**: p. 283-293.

98. Kutateladze, S. and I. Gogonin, *Growth rate and detachment diameter of a vapor bubble in free convection boiling of a saturated liquid.* TepVT, 1979. **17**: p. 792-797.

99. Stephan, K. and M. Abdelsalam, *Heat-transfer correlations for natural convection boiling.* International Journal of Heat and Mass Transfer, 1980. **23**(1): p. 73-87.

100. Jensen, M.K. and G.J. Memmel. *Evaluation of bubble departure diameter correlations*. in *International Heat Transfer Conference Digital Library*. 1986. Begel House Inc.

101. Chen, Y. and M. Groll, *Dynamics and shape of bubbles on heating surfaces: A simulation study.* International Journal of Heat and Mass Transfer, 2006. **49**(5-6): p. 1115-1128.

102. Van Helden, W., C. Van Der Geld, and P. Boot, *Forces on bubbles growing and detaching in flow along a vertical wall.* International journal of heat and mass transfer, 1995. **38**(11): p. 2075-2088.

103. Chen, D., L.-m. Pan, and S. Ren, *Prediction of bubble detachment diameter in flow boiling based on force analysis.* Nuclear engineering and design, 2012. **243**: p. 263-271.

104. Phan, H.T., et al., *A model to predict the effect of contact angle on the bubble departure diameter during heterogeneous boiling.* International Communications in Heat and Mass Transfer, 2010. **37**(8): p. 964-969.

105. Končar, B., I. Kljenak, and B. Mavko, *Modelling of local two-phase flow parameters in upward subcooled flow boiling at low pressure.* International Journal of Heat and Mass Transfer, 2004. **47**(6-7): p. 1499-1513.

106. Mazzocco, T., et al., *A reassessed model for mechanistic prediction of bubble departure and lift off diameters.* International Journal of Heat and Mass Transfer, 2018. **117**: p. 119-124.

107. Cole, R., *Bubble frequencies and departure volumes at subatmospheric pressures.* AIChE Journal, 1967. **13**(4): p. 779-783.

108. Hatton, A. and I. Hall. *Photographic study of boiling on prepared surfaces*. in *International Heat Transfer Conference Digital Library*. 1966. Begel House Inc.

109. Ivey, H., *Relationships between bubble frequency, departure diameter and rise velocity in nucleate boiling.* International Journal of Heat and Mass Transfer, 1967. **10**(8): p. 1023-1040.

110. Tu, J. and G. Yeoh, *On numerical modelling of low-pressure subcooled boiling flows.* International Journal of Heat and Mass Transfer, 2002. **45**(6): p. 1197-1209.

111. Lee, P., F. Tseng, and C. Pan, *Bubble dynamics in microchannels. Part I: single microchannel.* International Journal of Heat and Mass Transfer, 2004. **47**(25): p. 5575-5589.

112. Zuber, N., *Hydrodynamic aspects of boiling heat transfer*. 1959: United States Atomic Energy Commission, Technical Information Service.

113. Situ, R., et al., *Bubble departure frequency in forced convective subcooled boiling flow*. International Journal of Heat and Mass Transfer, 2008. **51**(25-26): p. 6268-6282.

114. Ishii, M. and N. Zuber, *Drag coefficient and relative velocity in bubbly, droplet or particulate flows.* AIChE journal, 1979. **25**(5): p. 843-855.

115. Basu, N., G.R. Warrier, and V.K. Dhir, *Wall heat flux partitioning during subcooled flow boiling: Part 1—model development.* J. Heat Transfer, 2005. **127**(2): p. 131-140.

116. Li, W., et al., *Enhanced flow boiling in microchannels using auxiliary channels and multiple micronozzles (I): Characterizations of flow boiling heat transfer*. International Journal of Heat and Mass Transfer, 2018. **116**: p. 208-217.

117. Yang, F., et al., *Enhanced flow boiling in microchannels by self-sustained high frequency two-phase oscillations.* International Journal of Heat and Mass Transfer, 2013. **58**(1-2): p. 402-412.

118. Li, W.M., et al., *Experimental and theoretical studies of critical heat flux of flow boiling in microchannels with microbubble-excited high-frequency two-phase oscillations*. International Journal of Heat and Mass Transfer, 2015. **88**: p. 368-378.

119. Kline, S.J. and F.A. McClintock, *Describing uncertainties in single-sample experiments.* Mechanical Engineering, 1953. **75**(1): p. 3- 8.

120. Euh, D., et al., *Characteristics of bubble departure frequency in a low-pressure subcooled boiling flow*. Journal of nuclear science and technology, 2010. **47**(7): p. 608-617.

121. Kuo, C.J., et al., *Bubble dynamics during boiling in enhanced surface microchannels.* Journal of Microelectromechanical Systems, 2006. **15**(6): p. 1514-1527.

122. Warrier, G.R. and V.K. Dhir, *Heat Transfer and Wall Heat Flux Partitioning During Subcooled Flow Nucleate Boiling—A Review.* Journal of Heat Transfer, 2006. **128**(12): p. 1243.

123. Naphon, P., *Effect of wavy plate geometry configurations on the temperature and flow distributions.* International Communications in Heat and Mass Transfer, 2009. **36**(9): p. 942-946.

124. Hung, T.-C., et al., *Optimal design of geometric parameters of double-layered microchannel heat sinks.* International Journal of Heat and Mass Transfer, 2012. **55**(11-12): p. 3262-3272.

125. Zhang, J., J. Kundu, and R.M. Manglik, *Effect of fin waviness and spacing on the lateral vortex structure and laminar heat transfer in wavy-plate-fin cores.* International Journal of Heat and Mass Transfer, 2004. **47**(8-9): p. 1719-1730.

126. Sui, Y., C.J. Teo, and P.S. Lee, *Direct numerical simulation of fluid flow and heat transfer in periodic wavy channels with rectangular cross-sections.* International Journal of Heat and Mass Transfer, 2012. **55**(1-3): p. 73-88.

127. Li, W., et al., *A Numerical Parametric Study of Flow and Heat Transfer in Circular and Zig-Zag Square Microchannel Heat Sinks.* 2016(50336): p. V002T15A015.

128. Ma, J., et al., *Realizing highly coordinated, rapid and sustainable nucleate boiling in microchannels on HFE-7100.* International Journal of Heat and Mass Transfer, 2019. **133**: p. 1219-1229.

129. Yang, F., X. Dai, and C. Li, *High frequency microbubble-switched oscillations modulated by microfluidic transistors.* Applied Physics Letters, 2012. **101**(7): p. 073509.

130. Kuo, C.-J., et al., *Bubble dynamics during boiling in enhanced surface microchannels.* Journal of Microelectromechanical Systems, 2006. **15**(6): p. 1514-1527.

131. Hetsroni, G., et al., *Two-phase flow patterns in parallel micro-channels.* International Journal of Multiphase Flow, 2003. **29**(3): p. 341-360.

132. Solomon, B.R., K.S. Khalil, and K.K. Varanasi, *Drag reduction using lubricant-impregnated surfaces in viscous laminar flow*. Langmuir, 2014. **30**(36): p. 10970-10976.